Impact of shell model interactions on nuclear responses to WIMP elastic scattering

R. Abdel Khaleq,[1,2,3,*] G. Busoni,[1,3,†] C. Simenel,[1,2,3,‡] and A. E. Stuchbery[2,3,§]

[1]*Department of Fundamental and Theoretical Physics, Research School of Physics, Australian National University, ACT 2601, Australia*

[2]*Department of Nuclear Physics and Accelerator Applications, Research School of Physics, Australian National University, ACT 2601, Australia*

[3]*ARC Centre of Excellence for Dark Matter Particle Physics, Australia*

(Received 11 December 2023; accepted 21 March 2024; published 22 April 2024)

Nuclear recoil from scattering with weakly interacting massive particles (WIMPs) is a signature searched for in direct detection of dark matter. The underlying WIMP-nucleon interactions could be spin and/or orbital angular momentum (in)dependent. Evaluation of nuclear recoil rates through these interactions requires accounting for nuclear structure, e.g., through shell model calculations. We evaluate nuclear response functions induced by these interactions for ^{19}F, ^{23}Na, ^{28,29,30}Si, ^{40}Ar, ^{70,72,73,74,76}Ge, ^{127}I, and ^{128,129,130,131,132,134,136}Xe nuclei that are relevant to current direct detection experiments, and estimate their sensitivity to shell model interactions. Shell model calculations are performed with the NuShellX solver. Nuclear response functions from nonrelativistic effective field theory are evaluated and integrated over transferred momentum for quantitative comparisons. We show that although the standard spin-independent response is barely sensitive to the structure of the nuclei, large variations with the shell model interaction are often observed for the other channels. Significant uncertainties may arise from the nuclear components of WIMP-nucleus scattering amplitudes due to nuclear structure theory and modeling. These uncertainties should be accounted for in analyses of direct detection experiments.

DOI: 10.1103/PhysRevD.109.075036

I. INTRODUCTION

The detection of dark matter (DM) remains one of the most heavily pursued goals in physics today, as its exact nature continues to elude our understanding [1–4]. Among the potential DM candidates that have been proposed, weakly interacting massive particles (WIMPs) [5–7], that are new elementary particles, not included in the Standard Model (SM) of particle physics, with a mass and interaction strength close to the ones of the electroweak interaction, have attracted significant interest. This class of candidates can naturally thermally produce DM in the early Universe in the right amount to match the observed DM density, assuming they have a self-annihilation cross section of a similar order to that arising from the weak force; this has been termed the "WIMP miracle".

WIMP searches include production in colliders [8], identification of their annihilation or decay in our Galaxy [9], as well as direct detection (DD) of scattering between DM and SM particles through nuclear recoil or through ionization of target atoms [3,6]. However, all DD experiments so far have reported a null result [10–12], with just one longstanding exception (DAMA/LIBRA [13]) that still requires independent confirmation.

Evaluating WIMP-nucleus interaction rates for direct detection experiments requires detailed knowledge of the astrophysical DM halo velocity distribution, beyond the standard model (BSM) inputs, as well as a microscopic description of the nuclear structure properties of the target nuclei. In particular, nuclear structure properties could have a strong impact on scattering rates [14]. This motivated recent studies within the context of nonrelativistic effective field theory (NREFT) [15,16] and chiral effective field theory (ChEFT) [17–22]. A third alternative approach can be found in [23].

The standard characterization of the WIMP-nucleus cross section involves both a spin-independent (SI) term and a spin-dependent (SD) one. Different DM direct detection experiments with varying targets [24–30] offer

*raghda.abdelkhaleq@anu.edu.au
†giorgio.busoni@anu.edu.au
‡cedric.simenel@anu.edu.au
§andrew.stuchbery@anu.edu.au

the possibility of probing different WIMP-nucleus interaction channels. The SI (respectively SD) response functions can be obtained from scalar and/or vector (axial-vector) effective field theory (EFT) relativistic Lagrangians. On the one hand, the SI cross section is proportional to $\sim A^2$, where A is the atomic mass number, making SI cross sections larger for heavier target nuclei. On the other hand, the SD response is probed by nuclei/isotopes which have unpaired nucleons [14]. It is expected to be strongly hindered for spin saturated nuclei (i.e., with even numbers of protons and neutrons) due to the Pauli exclusion principle.

Traditionally, the SI and SD responses are obtained assuming momentum independent interactions between a WIMP and nucleons. The underlying justification is that the WIMP is expected to be nonrelativistic with typical velocity $\sim 10^{-3}c$ while the target nucleus is at rest. However, Fitzpatrick *et al.* [15] argued that the relative velocity between the WIMPs and nucleons is dominated by the internal velocity of the nucleons in the nucleus, which is of the order of $\sim 10^{-1}c$. As a result, momentum-dependent operators should be considered, opening additional interaction channels involving the nucleon orbital angular momentum L. In addition to the standard SI and SD responses, one should then also consider an orbital angular momentum dependent (LD) response, as well as a response that depends both on spin and L (LSD). Note that these responses are evaluated within the NREFT for one-body currents [15,16,31], while ChEFT also predicts possible significant contributions from two-body currents [19], e.g., induced by WIMP scattering off virtual pions exchanged between two nucleons [17]. Corrections are also expected to the one-body currents due to the large Lorentz scalar and vector mean-fields present in the nucleus [32].

Recent progress in *ab initio* methods [33] and their application to DM direct detection [34–37] are promising. Indeed, even if the use of restricted valence spaces is sometimes needed, approximations and adjustments are in principle better controlled than in traditional shell model calculations. Nevertheless, the latter remain a standard tool to determine nuclear ground-state wave functions entering the evaluation of nuclear responses from scattering off WIMPs, as they often lead to good reproductions of low-energy nuclear levels and transition amplitudes [38]. There has been an increased effort to quantify the uncertainties in these theoretical shell model calculations using statistical approaches, to enhance comparisons with experimental data and aid in making further predictions (see for example [39] for *sd* shell model valence space nuclei, [40] for the *p* shell, as well as [41] for ^{136}Xe in the interacting shell model picture). However, the reliability of shell model calculations for evaluating operators that are relevant to WIMP-nucleus scattering needs to be evaluated. Indeed, the uncertainty on the NREFT couplings induced by nuclear structure inputs has been recently evaluated for xenon isotopes by comparing two shell model interactions, leading to an uncertainty of up to $\sim 50\%$ in some channels [42].

Here, we perform a systematic study of the sensitivity of the WIMP-nucleus elastic scattering amplitude to nuclear structure for ^{19}F, ^{23}Na, $^{28–30}$Si, ^{40}Ar, $^{70,72–74,76}$Ge, ^{127}I, and $^{128–132,134,136}$Xe target nuclei relevant to direct detection experiments. Shell model calculations are performed with various shell model nuclear interactions to obtain nuclear response functions. Variations of the magnitude of these nuclear response functions with the nuclear interaction are used to quantify the level of uncertainty that arises purely from the nuclear components of WIMP-nucleus interaction. This is important for mappings between theory and experiment in the context of DM direct detection, as such uncertainties could be comparable to other sources, and therefore may be non-negligible.

In Sec. II we provide an overview of the NREFT formalism adopted from [15,16] and the nuclear operators which are considered in the current work. Details of the nuclear shell model calculations are also presented and linked to the DM-nucleus scattering formalism. In Sec. III we discuss shell model predictions for typical nuclear structure observables in ^{19}F, ^{23}Na, and ^{127}I. Nuclear response functions calculated using different shell model interactions are presented in Sec. IV for all nuclei in consideration. We summarize the main results and conclude in Sec. V. The Appendixes contain further technical details. Analytical expressions for the nuclear response functions, together with additional results relevant to DM direct detection studies are provided in the supplemental material [43].

II. THEORETICAL BACKGROUND AND METHODS

A. DM-nucleus elastic scattering formalism

The NREFT approach to WIMP-nucleus scattering was adopted by Fitzpatrick *et al.* in [15,16]. This work included LD and LSD nuclear interaction responses, in addition to the standard SI and SD ones. These provide additional avenues for a DM particle to interact with a nucleus during a scattering process, and may be comparatively significant in magnitude relative to the SI and SD responses for particular isotopes. We provide the relevant NREFT elastic scattering formalism. For brevity we only state the most important information (additional expressions and definitions can be found in Appendix B and in [15,16]).

The EFT interaction Lagrangian consists of four-field operators of the form,

$$\mathcal{L}_{\mathrm{int}} = \sum_{N=n,p} \sum_i c_i^{(N)} \mathcal{O}_i \chi^+ \chi^- N^+ N^-, \tag{1}$$

where χ represents the dark matter field and N a nucleon field. In the nonrelativistic regime, only operators with terms up to second order in momentum transfer $\vec{q} = \vec{p}' - \vec{p}$

are included, where $\vec{p}'$ is the outgoing χ momentum and $\vec{p}$ is the incoming counterpart. Most of the operators considered arise from the exchange of mediators of spin-1 or less [which are at most quadratic in either $\vec{S}$ (spin operator) or $\vec{v}$ ($\equiv \vec{v}_{\chi,\mathrm{in}} - \vec{v}_{N,\mathrm{in}}$)], while some operators employed do not arise from this traditional exchange. The Hamiltonian is Hermitian if it is constructed from the following operators:

$$i\vec{q}, \qquad \vec{v}^{\perp} \equiv \vec{v} + \frac{\vec{q}}{2\mu_N}, \qquad \vec{S}_\chi, \qquad \vec{S}_N, \tag{2}$$

where $\mu_N = m_N m_\chi/(m_N + m_\chi)$ is the reduced mass for the DM-nucleon system. Hence, the list of possible nonrelativistic operators is

$$\begin{aligned} &\mathcal{O}_1 = \mathbf{1}, \qquad \mathcal{O}_3 = i\vec{S}_N \cdot (\vec{q} \times \vec{v}^{\perp}), \qquad \mathcal{O}_4 = \vec{S}_\chi \cdot \vec{S}_N, \qquad \mathcal{O}_5 = i\vec{S}_\chi \cdot (\vec{q} \times \vec{v}^{\perp}), \\ &\mathcal{O}_6 = (\vec{S}_N \cdot \vec{q})(\vec{S}_\chi \cdot \vec{q}), \qquad \mathcal{O}_7 = \vec{S}_N \cdot \vec{v}^{\perp}, \qquad \mathcal{O}_8 = \vec{S}_\chi \cdot \vec{v}^{\perp}, \qquad \mathcal{O}_9 = i\vec{S}_\chi \cdot (\vec{S}_N \times \vec{q}), \\ &\mathcal{O}_{10} = i\vec{S}_N \cdot \vec{q}, \qquad \mathcal{O}_{11} = i\vec{S}_\chi \cdot \vec{q}, \qquad \mathcal{O}_{12} = \vec{S}_\chi \cdot (\vec{S}_N \times \vec{v}^{\perp}), \qquad \mathcal{O}_{13} = i(\vec{S}_N \cdot \vec{q})(\vec{S}_\chi \cdot \vec{v}^{\perp}), \\ &\mathcal{O}_{14} = i(\vec{S}_\chi \cdot \vec{q})(\vec{S}_N \cdot \vec{v}^{\perp}), \qquad \mathcal{O}_{15} = -(\vec{S}_\chi \cdot \vec{q})((\vec{S}_N \times \vec{v}^{\perp}) \cdot \vec{q}). \end{aligned} \tag{3}$$

The operator $\mathcal{O}_2 = (v^{\perp})^2$ is neglected as it is not obtained from the leading-order nonrelativistic reduction of the relativistic four-field $\mathcal{L}_{\mathrm{int}}$ terms in consideration. An additional operator $\mathcal{O}_{16} = -((\vec{S}_\chi \times \vec{v}^{\perp}) \cdot \vec{q}) \cdot (\vec{S}_N \cdot \vec{q})$ is also neglected as it is linearly dependent on $\mathcal{O}_{12}$ and $\mathcal{O}_{15}$. From the list of nonrelativistic interaction operators above, one can show that the DM-nucleus elastic scattering amplitude is written as a sum of the amplitudes of various nuclear operators, of the form,

$$\begin{aligned} \frac{1}{2J_i+1} \sum_{M_i, M_f} \left| \left\langle J_i M_f \left| \sum_{m=1}^{A} \mathcal{H}_{\mathrm{int}}(\vec{x}_m) \right| J_i M_i \right\rangle \right|^2 = \frac{4\pi}{2J_i+1} \Bigg[&\sum_{\{j,X\}} \sum_J^{\infty} |\langle J_i || l_j X_J(q) || J_i \rangle|^2 \\ &+ \sum_{\substack{\{j,X\};\{k,Y\};\{X,Y\} \\ X \neq Y}} \sum_J^{\infty} \mathrm{Re}[\langle J_i || l_j X_J(q) || J_i \rangle \langle J_i || l_k Y_J(q) || J_i \rangle^*] \Bigg], \end{aligned} \tag{4}$$

where $\mathcal{H}_{\mathrm{int}}$ is the interaction Hamiltonian, J_i is the nuclear ground-state angular momentum, A is the mass number, and $M_i(M_f)$ is the initial (final) angular momentum projection. Here, X and Y are one of six nuclear operators traditionally written as $M_{JM}, \Sigma''_{JM}, \Sigma'_{JM}, \Delta_{JM}, \Phi''_{JM}$, and $\tilde{\Phi}'_{JM}$. The treatment of these nuclear multipole operators here is familiar from work on semileptonic weak and electromagnetic interactions with nuclei, such as electron scattering [44–46], as well as neutrino reactions, charged lepton capture, and β decay [45,47], where a harmonic oscillator wave function basis was specifically employed to evaluate the single-particle matrix elements in [48]. The long-wavelength limit ($q \to 0$) gauges the type of interaction the operators are sensitive to (see Table I). M_{JM} is a SI operator, Σ''_{JM} and Σ'_{JM} are SD, and the remainder are l-dependent (LD), as well as $\vec{\sigma} \cdot \vec{l}$- and tensor-dependent (LSD) operators, respectively, where $\vec{l}$ is the orbital angular momentum and $\vec{\sigma}$ is the spin. The four DM scattering amplitudes $l_j, l_k \equiv l_{0,E,M,5}$, each associated with a specific nuclear operator X, are encoded with the DM and nuclear target physics alongside linear combinations of effective theory couplings. The cross terms in Eq. (4) exist only for

TABLE I. Leading-order terms of the nuclear operators in the long-wavelength limit $q \to 0$ [15].

Response type	Leading multipole	Long-wavelength limit
M_{JM}: Charge	$M_{00}(q\vec{x}_m)$	$\frac{1}{\sqrt{4\pi}} 1(m)$
L^5_{JM}: Axial longitudinal	$\Sigma''_{1M}(q\vec{x}_m)$	$\frac{1}{2\sqrt{3\pi}} \sigma_{1M}(m)$
T^{el5}_{JM}: Axial transverse electric	$\Sigma'_{1M}(q\vec{x}_m)$	$\frac{1}{\sqrt{6\pi}} \sigma_{1M}(m)$
T^{mag}_{JM}: Transverse magnetic	$\frac{q}{m_N} \Delta_{1M}(q\vec{x}_m)$	$-\frac{q}{2m_N\sqrt{6\pi}} l_{1M}(m)$
L_{JM}: Longitudinal	$\frac{q}{m_N} \Phi''_{00}(q\vec{x}_m)$	$-\frac{q}{3m_N\sqrt{4\pi}} \vec{\sigma}(m).\vec{l}(m)$
	$\frac{q}{m_N} \Phi''_{2M}(q\vec{x}_m)$	$-\frac{q}{m_N} \frac{1}{\sqrt{30\pi}} [x_m \otimes (\vec{\sigma}(m) \times \frac{\vec{\nabla}}{i})_1]_{2M}$
T^{el}_{JM}: Transverse electric	$\frac{q}{m_N} \tilde{\Phi}'_{2M}(q\vec{x}_m)$	$-\frac{q}{m_N} \frac{1}{\sqrt{20\pi}} [x_m \otimes (\vec{\sigma}(m) \times \frac{\vec{\nabla}}{i})_1]_{2M}$

two sets of operators, M_{JM}, Φ''_{JM}, and Σ'_{JM}, Δ_{JM}. The initial nuclear spins have been averaged over and final ones summed over, and the matrix element is written in reduced matrix element form using the Wigner-Eckart theorem (see Appendix B). The full form of Eq. (4) in terms of the operators is also provided in Eq. (B1).

In the context of elastic scattering theory we are only interested in the ground-state nuclear wave function $|J_i\rangle$. The nuclear matrix elements can be written as a product of single-nucleon matrix elements and one-body density matrix elements (OBDMEs) $\Psi^{J;\tau}_{|\alpha|,|\beta|}$ in the following way:

$$\begin{aligned}\left\langle J_i;TM_T\left\|\sum_{m=1}^{A}\hat{O}_{J,\tau}(q\vec{x}_m)\right\|J_i;TM_T\right\rangle &= (-1)^{T-M_T}\begin{pmatrix} T & \tau & T \\ -M_T & 0 & M_T\end{pmatrix}\left\langle J_i;T\vdots\vdots\sum_{m=1}^{A}\hat{O}_{J,\tau}(q\vec{x}_m)\vdots\vdots J_i;T\right\rangle \\ &= (-1)^{T-M_T}\begin{pmatrix} T & \tau & T \\ -M_T & 0 & M_T\end{pmatrix}\sum_{|\alpha|,|\beta|}\Psi^{J;\tau}_{|\alpha|,|\beta|}\langle|\alpha|\vdots\vdots\hat{O}_{J,\tau}(q\vec{x})\vdots\vdots|\beta|\rangle,\end{aligned} \tag{5}$$

where α and β are single-nucleon states given by the usual quantum numbers $\beta = \{n_\beta, l_\beta, j_\beta, m_{j_\beta}, m_{t_\beta}\}$, with the reduced state notation $|\beta| = \{n_\beta, l_\beta, j_\beta\}$. The nucleon-isospin state $t_\beta = t_\alpha = 1/2$ is implicit in the notation. The nuclear isospin is denoted by T and its projection M_T. The notation $\vdots\vdots$ denotes a matrix element reduced in both angular momentum and isospin using the Wigner-Eckart theorem. Additionally, $\tau = \{0, 1\}$ with $\hat{O}_{J,\tau} = \hat{O}_J \tau_3^\tau$ and τ_3 being the nucleon isospin operator. Hence, the $\tau = 0$ term corresponds to the isospin-independent component of the single-nucleon operator, with $\tau = 1$ corresponding to isospin-dependent counterpart.

The OBDMEs have the form

$$\Psi^{J;\tau}_{|\alpha|,|\beta|} \equiv \frac{\left\langle J_i;T\vdots\vdots\left[a^\dagger_{|\alpha|}\otimes\tilde{a}_{|\beta|}\right]_{J;\tau}\vdots\vdots J_i;T\right\rangle}{\sqrt{(2J+1)(2\tau+1)}}, \tag{6}$$

where $\tilde{a}_\beta = (-1)^{j_\beta - m_{j_\beta} + 1/2 - m_{t_\beta}} a_{|\beta|;-m_{j_\beta},-m_{t_\beta}}$ and $\otimes$ denotes a tensor product. The OBDMEs contain all of the relevant information about the nuclear ground state for each isotope in consideration. Varying aspects of the nuclear model may lead to different OBDME values, and hence to different values of the nuclear matrix elements. Gauging the sensitivity of these matrix elements to nuclear structure is the goal of this work.

B. Nuclear structure

The nuclear shell model is a configuration interaction approach to the nuclear many-body problem that is widely used to calculate eigenstates of the nuclear hamiltonian as well as nuclear observables [38]. In practice, shell model calculations are performed assuming a filled inert core and a valence space of few single-nucleon orbitals above this core. Here, nuclear shell model calculations are performed with NuShellX [49]. Among the program's user inputs is the valence (model) space as well as a possible valence space truncation. For each model space, a range of nuclear shell model interactions are provided, each predeveloped based on constrained fits to certain nuclear data.

For each isotope, changing the interaction used for a particular valence space truncation may provide different OBDMEs, which may impact the values of the nuclear matrix elements; this is the investigation that we undertake in the current work. We employ interactions which differ from those used in [15,16] and compare the two sets of results.

These $\Psi^{J;\tau}_{|\alpha|,|\beta|}$ values are then inserted into a predeveloped Mathematica package [16], which calculates the relevant observables associated with DM-nucleus scattering. The OBDME values used to perform the calculations in this work can be found in the supplementary material [43].

C. Nuclear response functions

The aforementioned Mathematica package [16] can be used to calculate nuclear response functions,

$$F^{(N,N')}_{X,Y}(q^2) \equiv \frac{4\pi}{2J_i+1}\sum_{J=0}^{2J_i}\langle J_i||X^{(N)}_J||J_i\rangle\langle J_i||Y^{(N')}_J||J_i\rangle, \tag{7}$$

where $N,N' = \{p,n\}$. We also define $F^{(N,N')}_X(q^2) \equiv F^{(N,N')}_{X,X}(q^2)$. These response functions single out the nuclear aspect of the scattering amplitude and can be used to carry out an investigation of the effect of nuclear structure on WIMP-nucleus elastic scattering. The proton and neutron nuclear operators are given by $X^{(p)}_J = \frac{1+\tau_3}{2}X_J$ and $X^{(n)}_J = \frac{1-\tau_3}{2}X_J$. We have $F^{(p,n)}_{X,Y}(q^2) = F^{(n,p)}_{X,Y}(q^2)$ only for the noninterference responses with $X = Y$.

Using a harmonic oscillator single-particle basis, the response functions take on expressions of the form $e^{-2y}p(y)$, where $p(y)$ is a polynomial with $y = (qb/2)^2$ and $b = 1/\sqrt{m_N\omega} \approx \sqrt{41.467/(45A^{-1/3} - 25A^{-2/3})}$ fm is the harmonic oscillator length parameter (m_N is the nucleon mass and ω is the oscillator frequency). Following [15], we define proton and neutron integrated form factor (IFF) values as

$$\int_0^{100\ \mathrm{MeV}} \frac{qdq}{2} F_{X(,Y)}^{(N,N)}(q^2), \quad (8)$$

in units of MeV^2. These IFF values are a proxy for the strength of each of the nuclear interaction channels, which depend on the unique nuclear structure of the isotope in consideration. The effect of increasing the upper limit of this integral on the IFF values of ^{127}I is touched upon in Sec. IV A.

III. SHELL MODEL CALCULATIONS

Before investigating nuclear responses, we compare shell model predictions of energy spectra and electromagnetic transitions against experimental values for ^{19}F, ^{23}Na, and ^{127}I. We provide similar comparisons for the remaining odd nuclei considered in this work in Appendix A.

A. ^{19}F and ^{23}Na

We use an unrestricted *sd* model space with single particle levels $1d_{5/2}, 2s_{1/2}, 1d_{3/2}$ for both protons and neutrons. The work of [15,16] uses the USD [50,51] nuclear shell model interaction, whereas here we use the USDB interaction. The latter has been fitted to the energies of 608 (states) of 77 nuclei with $21 \leq A \leq 40$ [52].

The ^{19}F and ^{23}Na experimental energy spectra are compared with the USD and USDB energy levels in Figs. 1 and 2, respectively. Only positive parity states are possible for the chosen model space, hence we do not include the experimental states with negative parity. The overall agreement between experiment and theory is good up to ~3 MeV in ^{19}F and up to ~5 MeV in ^{23}Na.

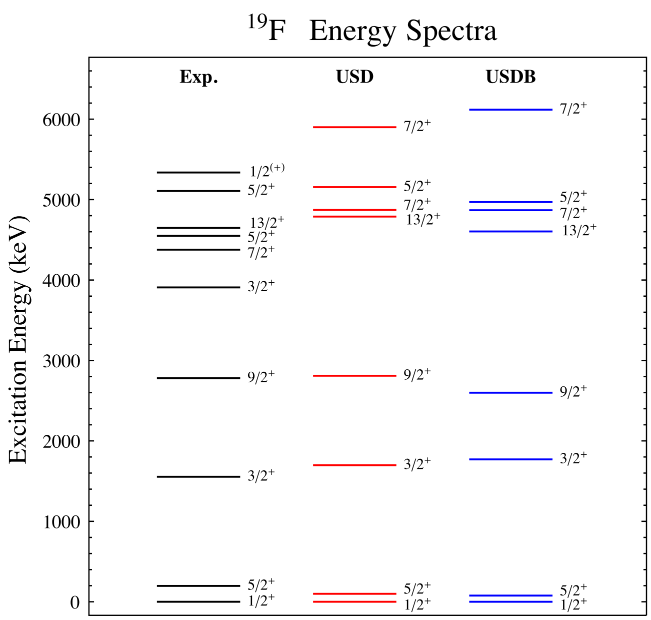

FIG. 1. ^{19}F energy levels (keV) from USD and USDB interactions in the *sd* model space are compared with experiment (only positive parity levels are shown).

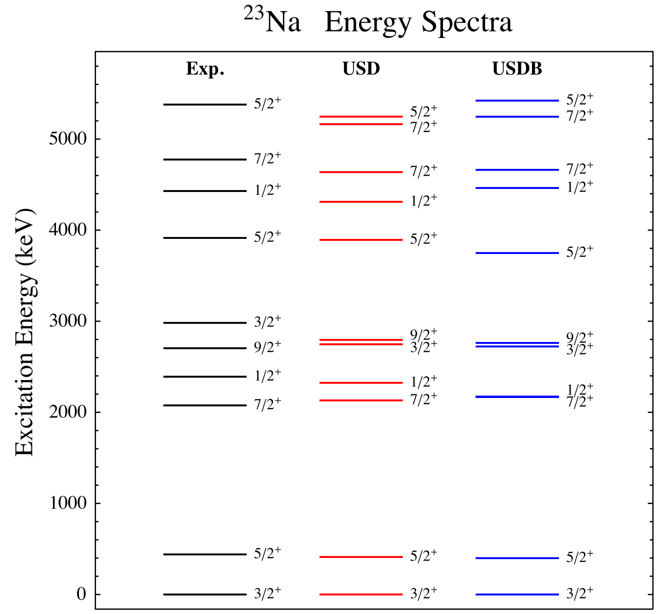

FIG. 2. Same as Fig. 1 for ^{23}Na.

As a test of the calculated nuclear matrix elements, Tables II and III provide a comparison between the theoretical and experimental electric quadrupole and magnetic dipole moments, as well as the electric quadrupole [B(E2)] and magnetic dipole [B(M1)] transitions between low-lying states. We note that the USD and USDB interactions were not fitted to such data. The default values of the effective charges and parameters of the $M1$ and $E2$ operators were used in the calculations. For ^{19}F and ^{23}Na, the proton and neutron effective charges are $e_p = 1.36$ and $e_n = 0.45$, respectively. The effective g factors take on values $g_{lp} = 1.137$, $g_{sp} = 4.94$, $g_{tp} = 0.34$, $g_{ln} = -0.079$, $g_{sn} = -3.38$, and $g_{tn} = -0.22$ for USD, whilst for USDB these are $g_{lp} = 1.174$, $g_{sp} = 5.00$, $g_{tp} = 0.24$, $g_{ln} = -0.11$, $g_{sn} = -3.44$, and $g_{tn} = -0.16$ (see Table I of Ref. [53]). Overall, both interactions lead to similar predictions and agree well with experimental data. As USDB is an extension of USD, the two interactions are expected to be similar for these stable isotopes. Both interactions are expected to produce realistic ground-state wave functions and could then be used to predict nuclear responses to WIMP-nucleon elastic scattering.

B. ^{127}I

The work of [15,16] utilizes a nuclear shell model interaction developed by Baldridge and Dalton [59], which we refer to as "B&D". This interaction is used in the model space which includes all proton and neutron orbits in the major shell between magic numbers 50 and 82, with single particle levels $1g_{7/2}$, $2d_{5/2}$, $2d_{3/2}$, $3s_{1/2}$, and $1h_{11/2}$.

TABLE II. Magnetic dipole and electric quadrupole moments of low-lying states of ^{19}F and ^{23}Na. Experimental moments taken from [54–56].

		Q [e fm^2]			μ [nm]		
	State	USD	USDB	Exp.	USD	USDB	Exp.
^{19}F	$1/2^+_{gs}$				+2.650	+2.681	+2.628[a]
	$5/2^+_1$	−9.53	−9.47	−9.42(9)	+3.504	+3.424	+3.605(8)
^{23}Na	$3/2^+_{gs}$	+11.0	+10.7	+10.4(1)	+2.194	+2.128	+2.218[a]

[a]The uncertainty is much less than ±0.001.

TABLE III. Electric quadrupole [B(E2)] and magnetic dipole [B(M1)] transitions between low-lying states of ^{19}F and ^{23}Na. Experimental transition values are from [57,58].

		B(E2) [e^2 fm^4]			B(M1) [nm^2]		
	Transition	USD	USDB	Exp.	USD	USDB	Exp.
^{19}F	$5/2^+_1 \to 1/2^+_{gs}$	19.22	19.44	20.93(24)			
	$3/2^+_1 \to 5/2^+_1$	8.068	7.986		3.03	3.19	4.1(25)
	$9/2^+_1 \to 5/2^+_1$	18.82	19.32	24.7(27)			
^{23}Na	$5/2^+_1 \to 3/2^+_{gs}$	109.2	109.1	124(23)	0.361	0.357	0.403(25)
	$7/2^+_1 \to 5/2^+_1$	61.72	57.03	56.7(85)	0.262	0.238	0.294(34)
	$1/2^+_1 \to 5/2^+_1$	10.31	14.48	11.3(27)			

The valence space restriction employed in [15,16] involves fixing the occupation number of $1h_{11/2}$ to the minimum allowed nucleon number.

Here, we consider the SN100PN [60] and GCN5082 [61] interactions. Both begin with renormalization of the G matrix based on a nucleon-nucleon potential. The GCN5082 interaction began with the Bonn-C potential and was then fitted to about 400 low-lying energy levels of 80 nuclei with $50 \leq Z, N \leq 82$ by varying various combinations of two-body matrix elements. The SN100PN interaction was based on the CD-Bonn nucleon-nucleon interaction, with the renormalization of the G matrix carried to third order [62]. No fitting was performed, but the single-particle energies were set by reference to the energy levels of ^{133}Sb and ^{131}Sn. Differences between these two interactions represent the theoretical uncertainty in our shell model calculations.

Our shell model calculations are performed in the same model space as the B&D calculations of [15,16], but with different restrictions. We keep the proton valence space levels $1g_{7/2}$ and $2d_{5/2}$ unrestricted, with a maximum of two protons in the rest. The neutron valence space is unrestricted for the $2d_{3/2}$, $3s_{1/2}$, and $1h_{11/2}$ levels, with a full $2d_{5/2}$ level and a minimum of six neutrons in $1g_{7/2}$. Restrictions were needed to keep the basis space within the memory limits imposed by NuShellX. Nevertheless, the restrictions we have used are chosen to pick out the dominant configurations in the full-space wave function.

The ^{127}I energy levels predicted by the SN100PN and GCN5082 interactions are plotted in Fig. 3 and compared with experimental data. The ordering of the first three experimental levels is not reproduced by either interaction.

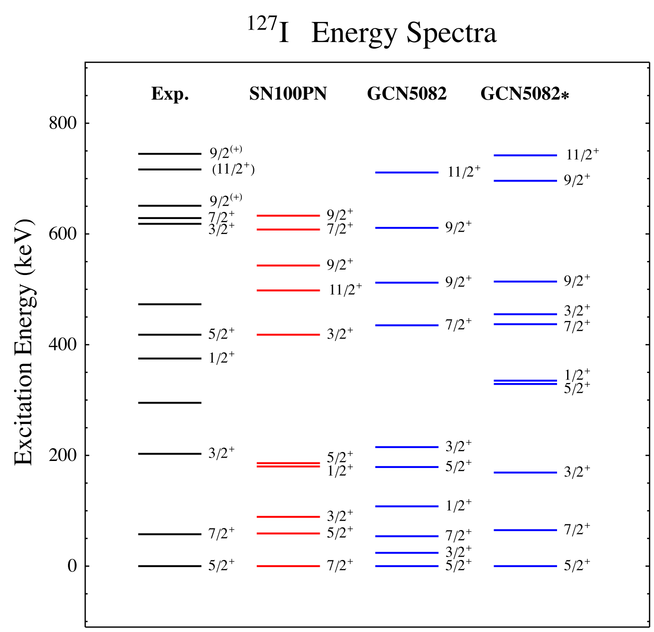

FIG. 3. ^{127}I energy spectra (keV) for experimental data, as well as the SN100PN and GCN5082 interactions in a restricted model space. GCN5082* refers to GCN5082 Expanded.

TABLE IV. Magnetic dipole and electric quadrupole moments of low-lying states of ^{127}I. Experimental moments are taken from [54–56]. GCN5082* refers to GCN5082 Expanded.

	μ [nm]				Q [$e\,\mathrm{fm}^2$]			
State	GCN5082	GCN5082*	SN100PN	Exp.	GCN5082	GCN5082*	SN100PN	Exp.
$5/2_1^+$	+2.8920	+3.1284	+2.6046	+2.8087(14)	−49.85	−36.41	−58.96	−68.8(10)
$7/2_1^+$	+2.29	+2.75	+2.38	+2.54(5)	−63.83	−33.38	−50.40	−61.7(11)
$3/2_1^+$	+1.45	+1.48	+1.35	+0.97(7)	+30.19	+40.85	+42.87	

The calculations also compress the energy spectrum compared with what is observed experimentally. This compression (prediction of excited states at too low an excitation energy) is often a consequence of the truncation of the basis space, where the omission of many small components of the wave function can lead to the prediction of the ground state and low-lying states at too high an energy (on an absolute scale). However, the lowest few states have the same spin-parity in theory and experiment, which gives confidence that the calculated wave functions in the restricted basis at least pick up the main components of a calculation without truncation.

Table IV provides a comparison between theoretical and experimental magnetic dipole and electric quadrupole moments for low-lying states. The effective charges and g factors used here are as adopted in recent studies of neighboring nuclei (see for example [63]). They specifically take on values of $e_p = 1.7$ and $e_n = 0.8$, as well as $g_{lp} = 1.130$, $g_{sp} = 3.910$, and $g_{sn} = -2.678$ for both SN100PN and GCN5082. Both interactions are in relatively good agreement with experiment. The spin-parity of the ground state being experimentally assigned to $5/2^+$, it is appropriate to use the first $5/2^+$ predicted by the shell model calculations in the computation of nuclear response in WIMP-nucleus elastic scattering. GCN5082 correctly predicts this state to be the ground state, while with SN100PN it is the first excited state. The two interactions appear to be performing with a similar level of accuracy as one another, with respect to the experimental expectations. The differences are useful in our study as it is anticipated that they may translate into different nuclear responses to WIMP-nucleus elastic scattering. Hu *et al.* have indeed found large theoretical uncertainties in ^{127}I structure factors for SD scattering [37].

IV. NUCLEAR RESPONSE FUNCTIONS

It is clear from the previous discussion that strong variations of nuclear response functions with the underlying shell model interactions are expected in the case of ^{127}I. We then focus first on this isotope before presenting systematic studies of integrated form factors. Note that, in the following, the $\tilde{\Phi}'$ response is included for completeness. It is however not discussed in detail as it is an exotic response induced purely by unusual couplings of WIMPs [15].

A. ^{127}I

The response functions $F_X^{(p,p)}(q^2)$ (solid lines) and $F_X^{(n,n)}(q^2)$ (dashed lines) are shown in Fig. 4 for the nuclear operators $X = M$, Δ, Σ', Σ'', Φ'', and $\tilde{\Phi}'$. The response functions obtained from the Mathematica notebook of [16] (i.e., not the approximated ones published in their manuscript) with the B&D interaction are reported together with the SN100PN and GCN5082 results from the present work (see Sec. III B for details on the valence space truncation). The Helm response [64] is also plotted for comparison with the SI responses in Fig. 5, which has the form $F(q) = 3e^{-(qs)^2/2}(\sin(qr_n) - qr_n\cos(qr_n))/(qr_n)^3$, with nuclear skin thickness $s \approx 0.9$ fm and nuclear radius $r_n^2 = ((1.23A^{1/3} - 0.6)^2 + (7/3)\pi^2(0.52)^2 - 5(s/\mathrm{fm})^2)\,\mathrm{fm}^2$. All calculations agree up to $q \sim 120$ MeV, beyond which they differ in value.

The spin-independent response $F_M^{(N,N)}(q^2)$ is barely sensitive to the choice of interaction. Although all interactions predict similar shapes for the orbital angular momentum dependent responses $F_\Delta^{(N,N)}(q^2)$, significant variations in magnitude are observed, of the order of 25–45% for the larger differences at low q. These variations are significantly larger for the other channels involving a spin dependence (Σ', Σ'', Φ'', $\tilde{\Phi}'$).

In almost all cases, however, all interactions agree on the respective importance of proton and neutron contributions. At low q, the spin-independent responses F_M are simply proportional to the square of the number of protons and neutrons. F_Δ, $F_{\Sigma'}$, and $F_{\Sigma''}$ responses are largely dominated by protons. Indeed, ^{127}I has an odd number of protons and an even number of neutrons. Spin and orbital angular momentum are likely to be canceled in nucleon pairs, leaving these contributions dominated by the unpaired proton.

In the long-wavelength approximation Φ'' reduces in part to the spin-orbit operator (see Table I). The latter can lead to coherent contributions that are maximized when one spin-orbit partner is fully occupied and the other one empty. In ^{127}I for SN100PN and GCN5082, these contributions are dominated by the proton $1g_{9/2,7/2}$ and neutron $1h_{11/2,9/2}$ spin-orbit partners. Indeed, $1g_{9/2}$ belongs to the core and is

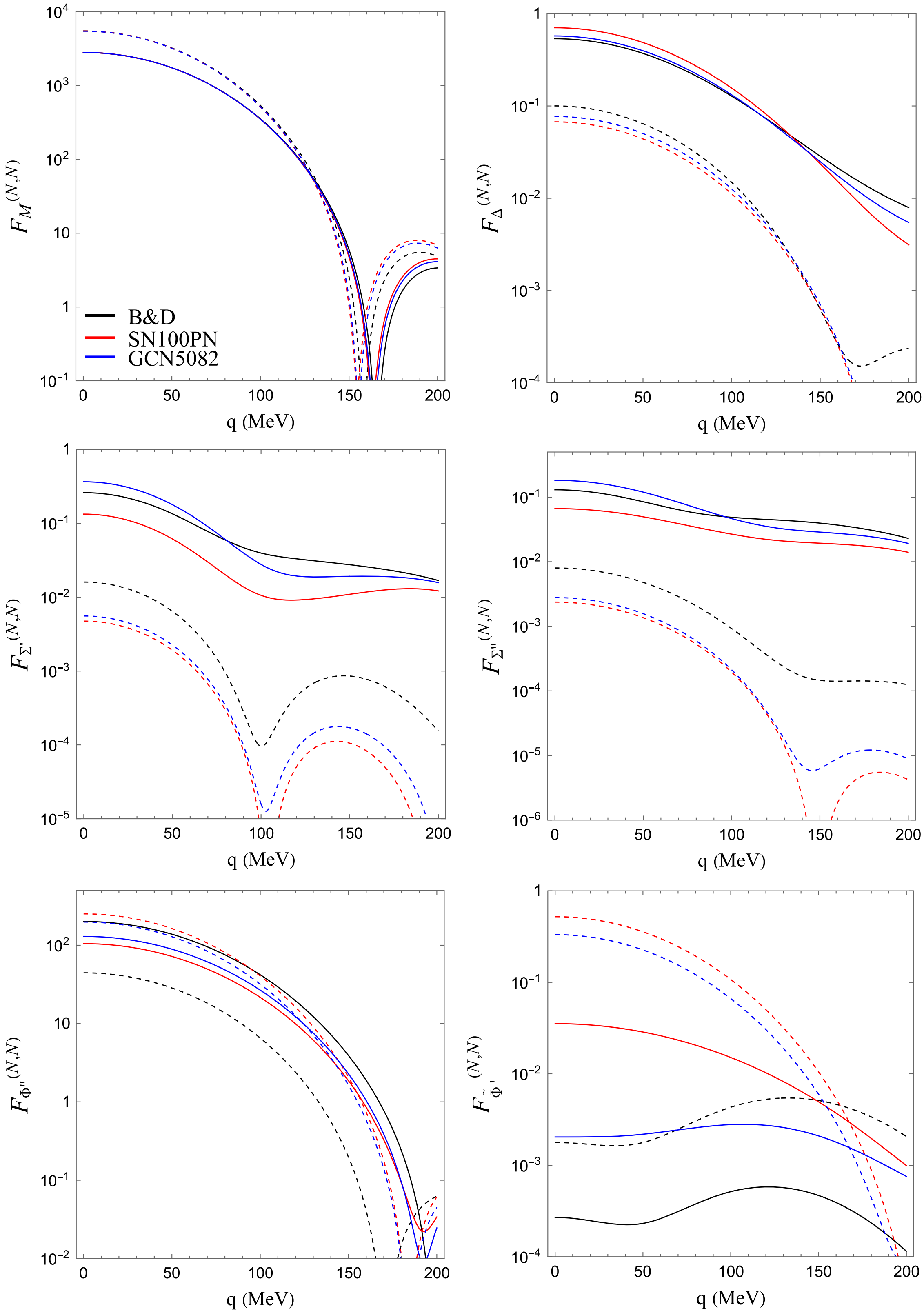

FIG. 4. ^{127}I proton-proton (solid lines) and neutron-neutron (dashed lines) nuclear response functions $F_X^{(N,N)}(q^2)$ obtained with three different shell model interactions. The B&D results are from [16].

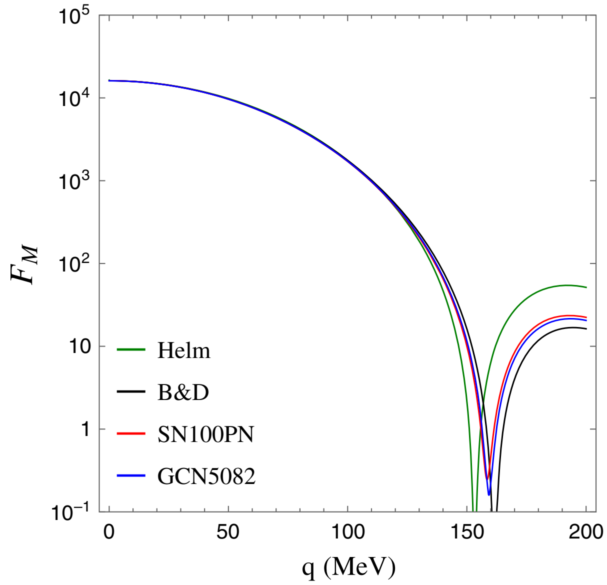

FIG. 5. ^{127}I SI nuclear response function $F_M(q^2)$ obtained with three different shell model interactions, with the Helm response plotted for comparison.

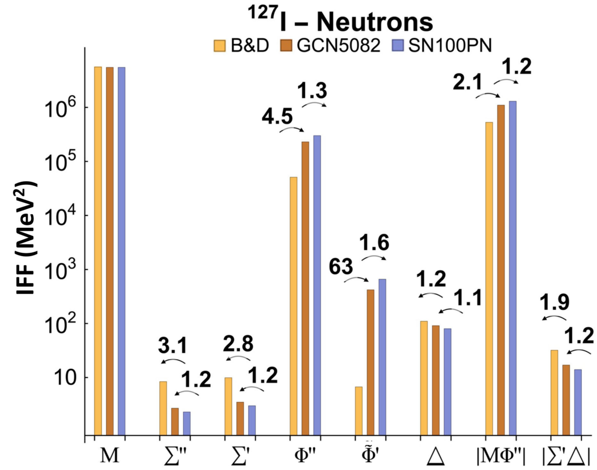

FIG. 7. Same as Fig. 6 for ^{127}I neutron IFF.

thus fully occupied, with at most three protons in $1g_{7/2}$, while $1h_{9/2}$ is above the valence space and thus empty, with at least four neutrons in $1h_{11/2}$. These coherent effects can amplify differences coming from the various approximations used in the shell model calculations. In particular, we see that the calculations of [16] with the B&D interaction predict a very small neutron contribution to the Φ'' operator. This is likely due to the fact that they fix the occupation of $1h_{11/2}$ to its minimum (four neutrons), while in our calculations this value can be larger, thus leading to stronger neutron contribution in our case.

Figures 6 and 7 show the proton and neutron IFF values [see Eq. (8)], respectively, for the three shell model interactions. Although we choose to represent all IFFs for either protons or neutrons on the same figure, one should refrain from using them to compare the relative importance of each response. Indeed, each IFF only reflects the ability of the nucleus to interact through a specific channel. Whether WIMPs are themselves able to probe this channel depends on the particle physics model that translates into the coefficients c_i in Eq. (1). Nevertheless, for simplicity, and assuming that these c_i coefficients are of a similar order, the SI (M) channels will be considered to be the leading responses, while subleading responses include the LSD (Φ'') channel (due to the coherent contribution from partially occupied spin-orbit partners) as well as the SD (Σ' and Σ'') and LD (Δ) channels in nuclei with odd protons or neutron numbers.

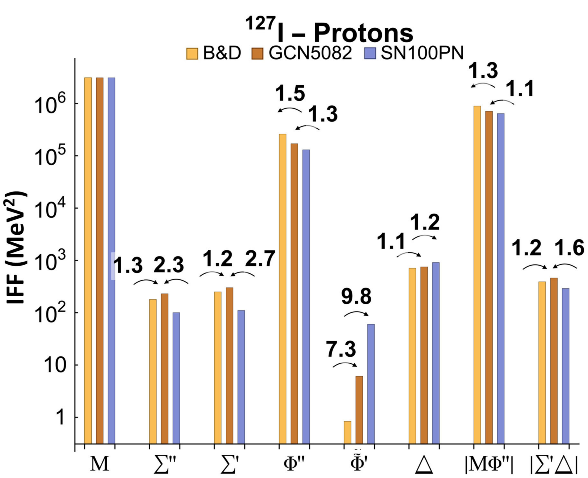

FIG. 6. ^{127}I proton IFF values in units of (MeV)^2, evaluated using Eq. (8).

Large variations are observed in almost all subleading channels, e.g., SD proton (Σ'_p, Σ''_p), LD proton (Δ_p), LSD ($\Phi''_{p,n}$), and their interferences, including with the SI response ($M_{p,n}$). The largest of these variations reach a factor ∼5 between B&D and the other interactions for the Φ''_n response. These differences are considered reasonably significant, especially in comparison with those found in lighter nuclei, e.g., ^{19}F.

To evaluate the effect of valence space truncation on the nuclear IFF values, we repeated our shell model calculation for ^{127}I with the SN100PN interaction using a stricter valence space truncation for neutrons, with no further restriction imposed on the proton valence space. The neutron valence space is still unrestricted for the $2d_{3/2}$ and $3s_{1/2}$ levels, and the $2d_{5/2}$ level is still fully occupied. However, the $1g_{7/2}$ is now assumed to be full (instead of having a minimum of six neutrons), and $1h_{11/2}$ is restricted to a maximum of eight neutrons (instead of being unrestricted). There is an overall of six neutron single particle states (two occupied and four empty) that have been restricted compared to the previous calculation.

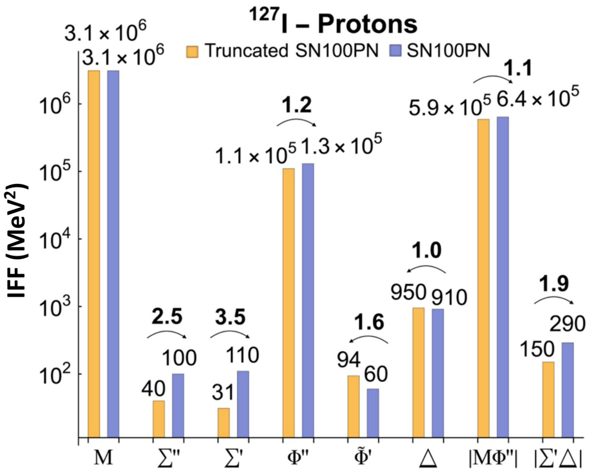

FIG. 8. Same as Fig. 6 for different SN100PN valence space truncation.

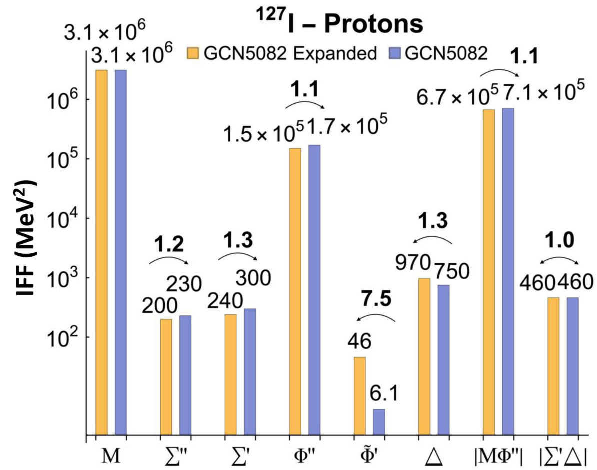

FIG. 10. Same as Fig. 6 for different GCN5082 valence space truncation.

The resulting IFFs are plotted in Figs. 8 and 9 for protons and neutrons, respectively. The effect remains relatively small for some subdominant responses such as $\Phi''_{p,n}$ (less than 20% variation), whereas some other channels exhibit larger differences, such as the proton SD channels, although they are much smaller in magnitude. When possible, the less restricted valence space should be used to evaluate nuclear response functions and limit uncertainties on the subleading channels.

We performed a second GCN5082 calculation, named "GCN5082 Expanded", which employs an alternative truncation compared to our original calculation above. The protons were restricted to a maximum of one proton excited out of the $1g_{7/2}$ and $2d_{5/2}$ subshells into the $2d_{3/2}, 3s_{1/2}$, and $1h_{11/2}$ subshells. Additionally, no more than two neutrons were excited out of the $1g_{7/2}$, and $2d_{5/2}$ subshells into the $2d_{3/2}, 3s_{1/2}$, and $1h_{11/2}$ subshells. In comparison with the previous restriction, this truncation allows for a maximum of two neutrons to leave both the $1g_{7/2}$ and $2d_{5/2}$ subshells, whereas previously the two neutrons were only allowed to leave the $1g_{7/2}$ level.

This new truncation scheme has a significant impact on the energy spectrum, as seen in Fig. 3. The new spectrum is much more aligned with experiment, with the ordering and spacing between the first three levels improved, and is now comparable with the low-lying states obtained by [21]. The entire spectrum is also less compressed compared to previous calculations, which is primarily due to the opening up of the $2d_{5/2}$ level. The theoretical electric quadrupole and magnetic dipole moments for this calculation are given in Table IV. The magnetic moments for this calculation remain in reasonable agreement with experimental values. However, the electric moments overall seem to be less in agreement with experiment compared to the previous GCN5082 calculation.

The IFF values comparing the GCN5082 Expanded calculation with the original are provided in Figs. 10

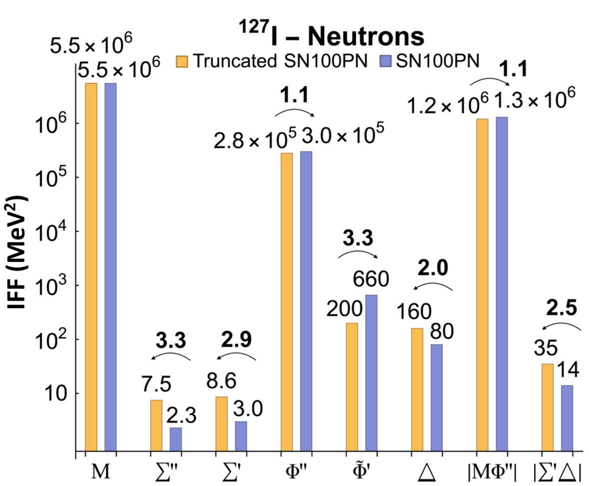

FIG. 9. Same as Fig. 7 for different SN100PN valence space truncation.

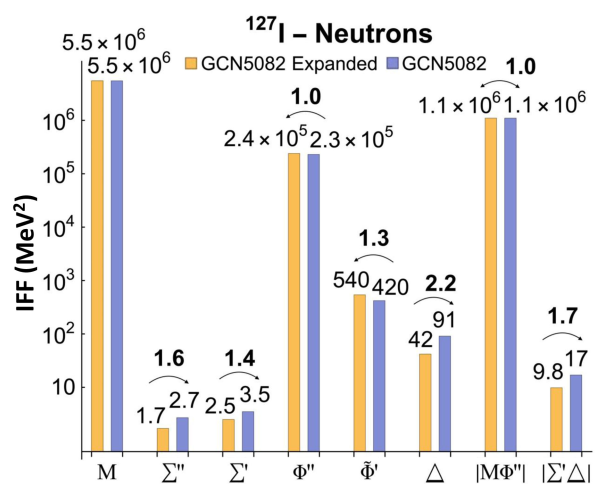

FIG. 11. Same as Fig. 7 for different GCN5082 valence space truncation.

and 11 for protons and neutrons respectively. The subleading proton and neutron Φ'' channels have small differences of $\lesssim 10\%$, whereas the subleading proton Σ', Σ'', and Δ channels exhibit differences of $\sim 20\%$–30%. Although these differences are non-negligible, they are not of the same order obtained from the Truncated SN100PN case, where here a more truncated valence space has a bigger effect on the IFF values for ^{127}I.

The IFF values change by a factor of 1.1–2.5 with $q_{\max} = 200$ MeV. Although the IFF variations with the shell model interaction remain of the same order, the magnitude of the SD variation sometimes depends on $q_{\max}$. Hence, quantitative studies for a specific experiment should account for the q range adapted to that experiment.

B. Systematic study of integrated form factors

Nuclear responses were computed for a range of isotopes relevant to DM direct detection: ^{19}F, ^{23}Na, ^{28,29,30}Si, ^{40}Ar, ^{70,72,73,74,76}Ge, ^{127}I, and ^{128,129,130,131,132,134,136}Xe. Analytic expressions for the momentum dependent response functions are provided in supplementary material [43]. In the following, IFFs are used to evaluate quantitative variations induced by the choice of the nuclear interaction for each specific model space. For elements with more than one stable isotope, IFFs have been weighted by the natural abundances of each isotope. Note that isotopes with even numbers of protons and neutrons only probe the M (SI) and Φ'' (LSD) responses as their ground states have spin-parity 0^+. The results are grouped and discussed with respect to valence space (and therefore interactions) used for the shell model calculations. In all cases the SI ($M_{p,n}$) IFF values are not affected by the choice of interaction and thus we focus the discussion on the subleading channels. Only nonzero IFF values are shown in the figures. All isotopes probe the M and Φ'' channels (as well as their interference), however only isotopes with ground state $J_i \geq 1/2$ can additionally probe the Σ'', Σ', and Δ channels, with $J_i \geq 1$ isotopes probing $\tilde{\Phi}'$.

1. ^{19}F, ^{23}Na, *and* ^{28,29,30}Si

We consider the same *sd* model space for ^{19}F, ^{23}Na, and silicon isotopes as described in Sec. III A. Proton and neutron IFF values are shown in Figs. 12–15 for ^{19}F and ^{23}Na, respectively. Both ^{19}F and ^{23}Na have a subleading spin-dependent proton response due essentially to their unpaired proton, while their spin-dependent neutron responses are orders of magnitude smaller. Although both USD and USDB predict similar responses for Σ'_p and Σ''_p in ^{19}F, about 20% differences are found in ^{23}Na.

The orbital angular momentum dependent (LD) response Δ in ^{19}F and ^{23}Na is also hindered for neutrons, though this hindrance is not as strong as in the SD case. The IFF for Δ is maximum for the ^{23}Na proton response, indicating that this nucleus could be a good candidate to probe this

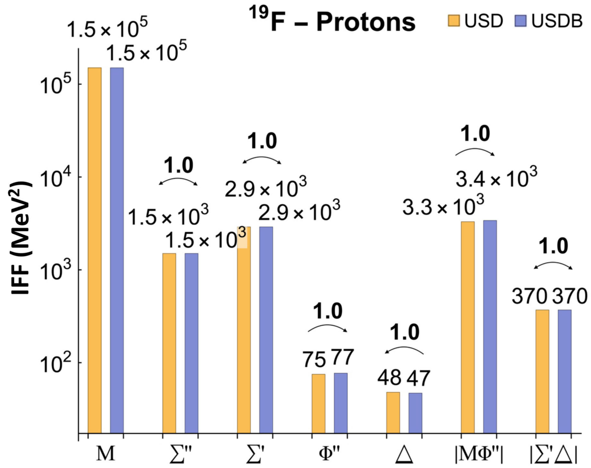

FIG. 12. Same as Fig. 6 for ^{19}F proton IFF.

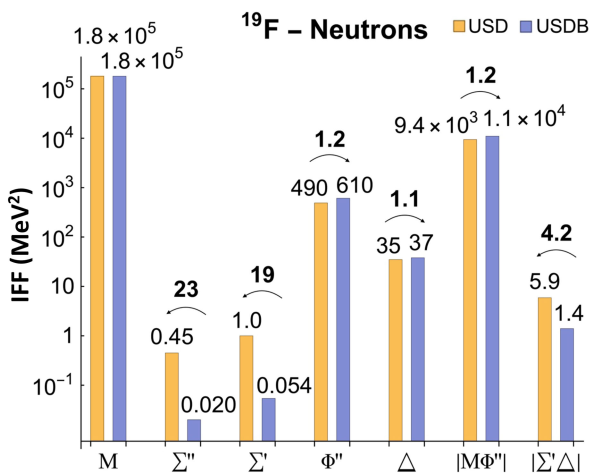

FIG. 13. Same as Fig. 6 for ^{19}F neutron IFF.

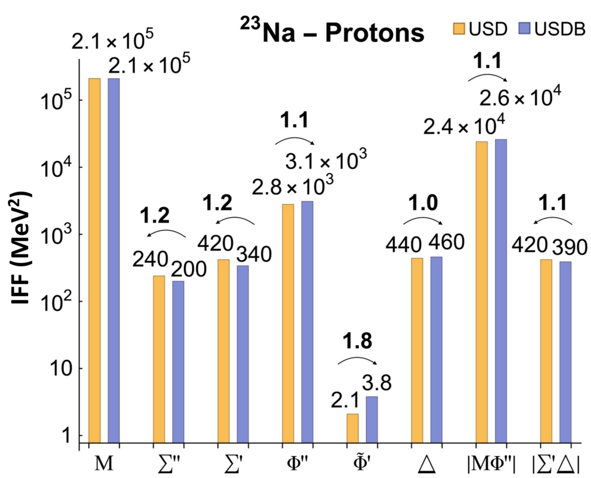

FIG. 14. Same as Fig. 6 for ^{23}Na proton IFF.

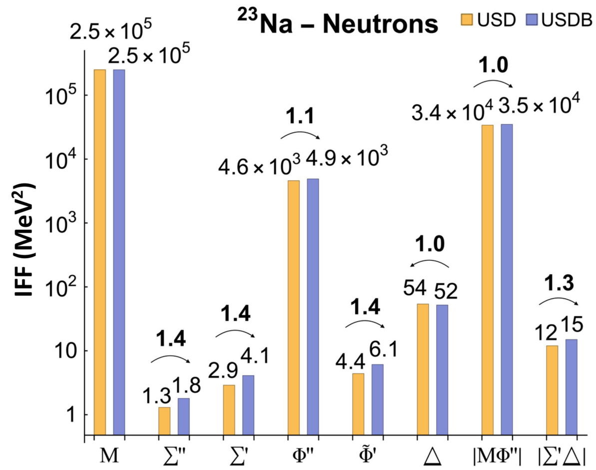

FIG. 15. Same as Fig. 6 for ^{23}Na neutron IFF.

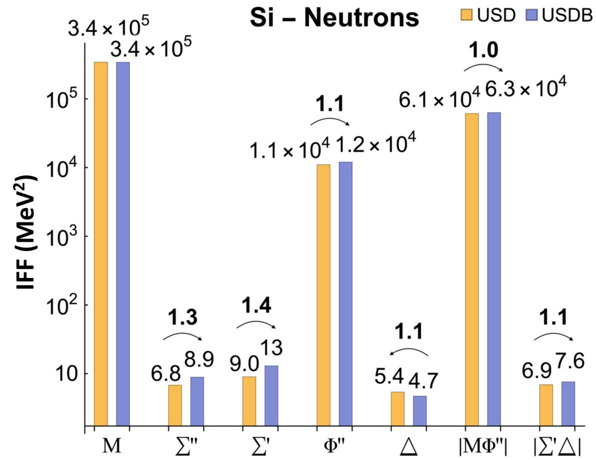

FIG. 17. Same as Fig. 6 for silicon neutron IFF.

channel. The results for this response are also stable with respect to the interaction, with a variation of only few % between USD and USDB predictions.

The LSD response in this valence space is dominated by the spin-orbit partners $1d_{5/2,3/2}$ and increases with increasing occupation of $1d_{5/2}$ as long as $1d_{3/2}$ remains comparatively lowly occupied (see supplementary material [43]). As a result, the IFF value of Φ'' in ^{19}F and ^{23}Na increases with the number of valence nucleons (one proton and two neutrons in ^{19}F, and three protons and four neutrons in ^{23}Na). Here, the impact of the interaction is non-negligible, with a maximum variation of $\sim$25% between USD and USDB in the ^{19}F neutron response. Indeed, providing no or small momentum dependence of these variations, they should translate directly into variations in WIMP-nucleus cross sections.

The IFF values for silicon are shown in Figs. 16 and 17 for protons and neutrons, respectively. We note that since ^{28}Si and ^{30}Si have ground states 0^+, they only probe the M, Φ'', and $|M\Phi''|$ channels, whereas ^{29}Si $(1/2^+)$ probes all except for $\tilde{\Phi}'$. The only subleading channel is the LSD response Φ'' and its interference with the SI channel M. Both interactions predict corresponding IFF values within few %. These IFF values are similar for both protons and neutrons as the most abundant isotope, ^{28}Si ($\sim$92%), has the same number of protons and neutrons. The $\Phi''_{p,n}$ IFF are also larger than in ^{19}F and ^{23}Na as ^{28}Si has six protons and six neutrons in the sd valance space, allowing for a configuration in the ground-state wave function with more full occupation of $1d_{5/2}$ while $1d_{3/2}$ remains comparatively poorly occupied (see Ref. [43]), thus maximizing the spin-orbit contribution. Silicon detectors should then be optimum for the LSD response in this mass region. Note also that the SD and LD responses are orders of magnitude larger for neutrons than for protons due to the unpaired neutron in ^{29}Si. However, its abundance ($\sim$4.7%) is too small for these channels to be subleading.

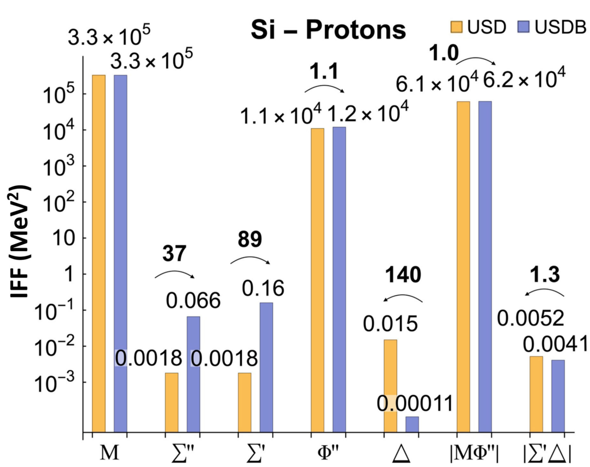

FIG. 16. Same as Fig. 6 for silicon proton IFF.

2. ^{40}Ar

Shell model calculations for ^{40}Ar have been performed in the $sdpf$ valence space with single particle levels $1d_{5/2}$, $2s_{1/2}$, $1d_{3/2}$, $1f_{7/2}$, $2p_{3/2}$, $1f_{5/2}$, and $2p_{1/2}$. A valence space truncation has been employed where the protons are unrestricted in the sd shell and blocked from entering the pf shell, while neutrons fill the sd shell and are unrestricted in the pf shell. Several interactions are available for this model space, including SDPF-NR [65], SDPF-U [66], EPQQM [67], and SDPF-MU [68]. Although we performed shell model calculations with all four interactions, we only provide the IFF values for the EPQQM and SDPF-MU interactions in Fig. 18 as they display the largest differences. This isotope was not considered in the work of [15,16].

The LSD proton and neutron subleading responses Φ'' are of the same order as that of ^{23}Na, and about half that of silicon. As for these nuclei, the proton Φ'' response is due to the $1d_{5/2,3/2}$ spin-orbit partners. However, the proton contribution to the ground state in ^{40}Ar is now likely to

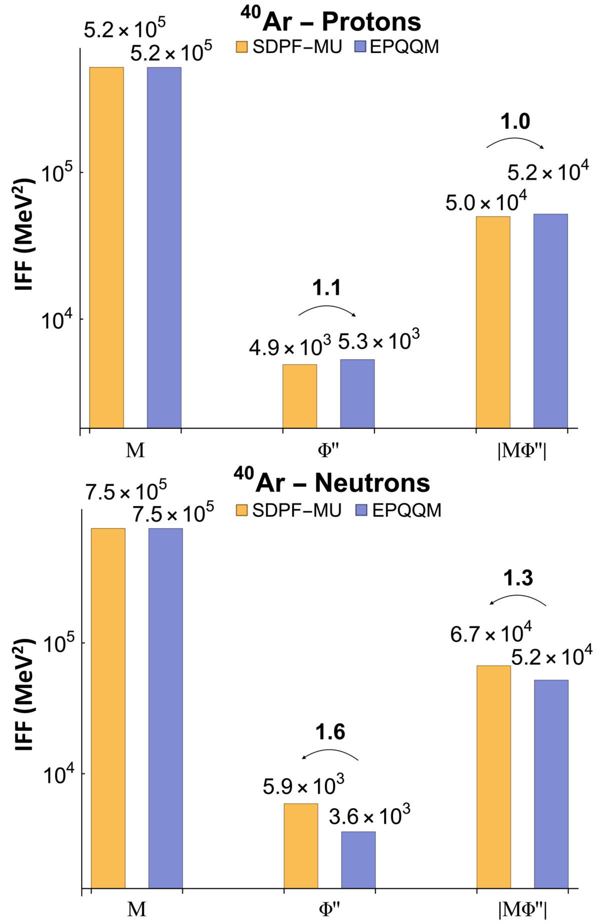

FIG. 18. Proton (top) and neutron (bottom) IFF values for ^{40}Ar with the SDPF-MU and EPQQM interactions in the restricted $sdpf$ valence space.

be dominated by a configuration with $1d_{5/2}$ fully occupied and $1d_{3/2}$ only half empty (see supplementary material for occupations of all valence levels [43]). The unavoidable partial occupation of $1d_{3/2}$ reduces the Φ'' response as compared to the optimum situation offered by silicon isotopes. For neutrons, both $1d_{5/2,3/2}$ levels are fully occupied and thus no contribution to Φ'' is expected from them. The latter is expected to come from the configuration with neutrons mostly distributed to the $1f_{7/2}$ level with its spin-orbit partner $1f_{5/2}$ comparatively unoccupied.

The absence of SD and LD responses implies that this target could be a good choice to isolate the SI and LSD responses. However, large variations are observed for the Φ'' subleading neutron response as well as in its interference with the SI response. In the proton case, the differences for all operators between all four interactions are much smaller as they do not exceed 10%.

3. ^{70,72,73,74,76}Ge

Shell model calculations for germanium isotopes were performed in the f_5pg_9 model space composed of the single-particle levels $2p_{3/2}$, $1f_{5/2}$, $2p_{1/2}$, and $1g_{9/2}$. The GCN2850 interaction [61] was used in [15,16] with a valence space truncation that consisted of limiting the occupation number of the $1g_{9/2}$ level to no more than two nucleons above the minimum occupation for all isotopes. In this work, we consider an unrestricted f_5pg_9 model space and employ the JUN45 [69] and jj44b [70] interactions.

The isotopic IFF values shown in Figs. 19 and 20 for protons and neutrons, respectively, are weighted according to natural abundance. ^{73}Ge is the only stable odd isotope and thus the only one to contribute to the Σ', Σ'', Δ, and $\tilde{\Phi}'$ responses. Due to its small abundance (7.8%), these responses remain relatively small, except for the neutron LD response Δ_n whose IFF is of the same order as, e.g., Δ_p in ^{23}Na. The large Δ_n response in ^{73}Ge is likely to be due to a strong contribution of the configuration with a partially occupied $1g_{9/2}$ level (with an orbital angular momentum of $4\hbar$) in the ground state (see supplementary material for occupations of all valence levels [43]).

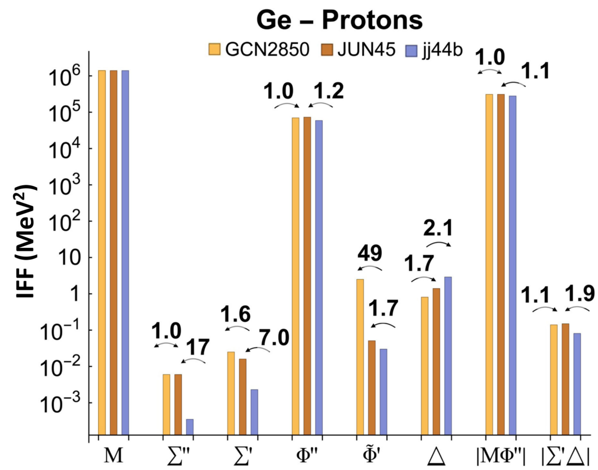

FIG. 19. Same as Fig. 6 for germanium proton IFF.

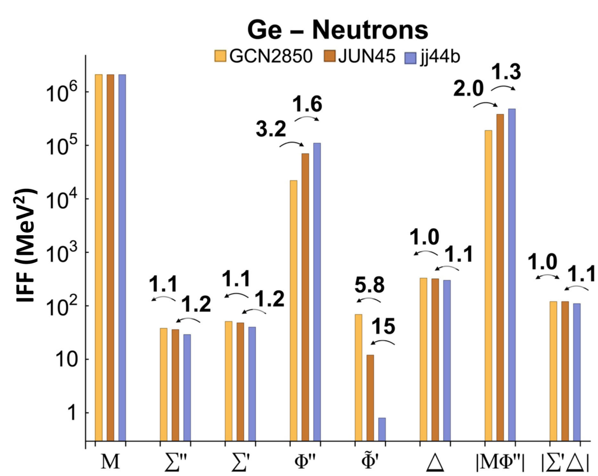

FIG. 20. Same as Fig. 6 for germanium neutron IFF.

The subleading proton LSD response is likely to be due to the $1f_{7/2,5/2}$ spin-orbit partners, with $1f_{7/2}$ fully occupied and $1f_{5/2}$ with a small occupation in the ground states. The interpretation of the neutron LSD response is more complicated as several isotopes contribute with similar abundances. In a single-particle picture, one would expect a small contribution as $1f_{5/2}$ would be full, the $2p_{1/2,3/2}$ spin-orbit partners only have a small angular momentum, and $1g_{9/2}$ only starts getting populated from ^{73}Ge. However, the single-particle picture is a crude approximation for mid-shell nuclei whose ground states are expected to be composed of mixed configurations. In particular, configurations in which $1f_{5/2}$ is not full or in which $1g_{9/2}$ has a nonzero occupation (while its spin-orbit partner $1g_{11/2}$ remains empty as it lies outside of the valence space) all contribute to Φ''.

As a result, the neutron LSD response is of the same order of magnitude as the proton one. However, uncertainties are much larger for neutrons (about a factor of 5 between GCN2850 and jj44b) than for protons where IFF predictions from different interactions vary by about 20%.

4. ^{127}I *and* ^{128,129,130,131,132,134,136}Xe

In addition to ^{127}I that is discussed in detail in Sec. IV A, shell model calculations have been performed with the SN100PN interaction [60] and within the same model space (see Sec. III B) for stable xenon isotopes with isotopic abundance greater than 1%. These isotopes have been studied in [15,16] with the B&D interaction [59]. Their work considered unrestricted ^{134}Xe and ^{136}Xe calculations, and their truncation for ^{128,130,132}Xe was identical to that of their ^{127}I calculation. Their truncation for ^{129}Xe and ^{131}Xe was further restricted by limiting the valence protons to the $2d_{5/2}$ and $1g_{7/2}$ levels whilst requiring neutrons to fully occupy these levels.

Here, we performed unrestricted calculations for ^{131,132,134,136}Xe, with ^{129}Xe and ^{130}Xe employing the same truncation as our original ^{127}I SN100PN calculation in Sec. III B. To make the ^{128}Xe calculation more feasible we further restrict the neutron valence space, by keeping the $2d_{3/2}$ and $3s_{1/2}$ levels unrestricted whilst completely filling the $1g_{7/2}$ and $2d_{5/2}$ levels, with a maximum of 8 neutrons in $1h_{11/2}$.

The xenon IFF values are shown in Figs. 21 and 22 for protons and neutrons, respectively. Comparing with ^{127}I IFF in Figs. 6 and 7, we see that SI (M) and LSD (Φ'') responses are of the same order due to their proximity in the nuclear chart. However, SD (Σ' and Σ'') and LD (Δ) responses are significantly different between both elements. Indeed, in ^{127}I they are dominated by the unpaired proton, while for xenon they are essentially induced by the unpaired neutrons in odd isotopes. Detectors with iodine and those with xenon are then complementary to investigate the proton and neutron SD and LD cross sections.

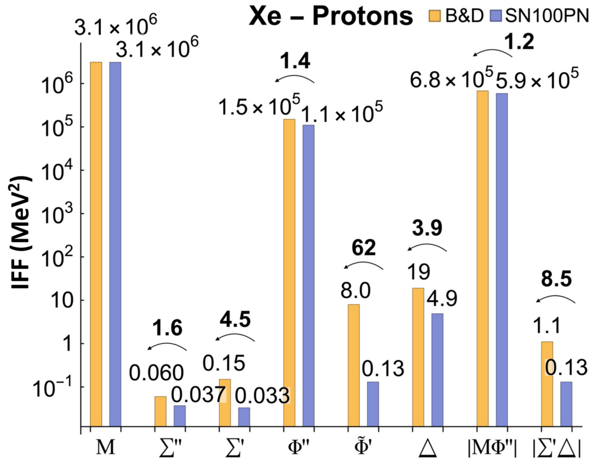

FIG. 21. Same as Fig. 6 for xenon proton IFF.

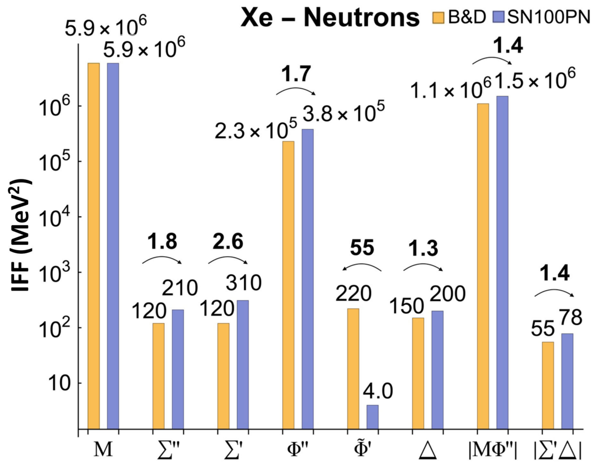

FIG. 22. Same as Fig. 6 for xenon neutron IFF.

However, strong variations are observed with respect to the interactions for all but the SI responses. The Φ'' proton responses vary by a factor $\sim$2 in ^{127}I ($\sim$40% in xenon) between B&D and SN100PN predictions. These variations are even larger for Φ'' neutron responses (factor $\sim$6 in ^{127}I and $\sim$65% in xenon). SD proton responses in ^{127}I vary by factors $\sim$2–3 with the interaction. Similar variations are observed in SD neutron responses in xenon. Variations for LD responses are somewhat smaller ($\sim$20–40% except for Δ_p in xenon which has a comparatively small IFF value).

V. DISCUSSION AND CONCLUSION

Nuclear shell model calculations have been performed with the NuShellX solver for isotopes relevant to direct detection experiments. The effect of nuclear structure on WIMP-nucleus elastic scattering is studied within the NREFT regime following [15,16]. IFF values were used as a proxy to evaluate nuclear response strength and the ability of the nuclei to interact via the six NREFT operators.

Except for the leading standard SI response, WIMP-nucleus scattering may be very sensitive to nuclear structure. The LSD Φ'' response is related to spin-orbit structures in the long wavelength limit and is maximum when one spin-orbit partner is fully occupied while the other is empty. It is expected to be more significant in heavier nuclei due to large spin-orbit splitting, larger orbital angular momentum l values, and higher degeneracies of the spin-orbit partners allowing for more nucleons to contribute coherently. The Σ'' and Σ' operators lead to the usual SD responses, and hence are more sensitive to isotopes with an odd number of protons (such as ^{19}F, ^{23}Na, and ^{127}I) or neutrons (e.g., odd isotopes of germanium and xenon). The Δ operator is l-dependent (in the long wavelength limit) and is larger for isotopes with unpaired nucleons in higher l orbits, such as ^{23}Na and ^{127}I for protons, and odd isotopes of germanium and xenon for neutrons. This dependence of the strength of the nuclear responses on the ground-state structure of each isotope means that different experimental efforts with various detection materials can probe different aspects of the WIMP-nucleus interaction.

The range of studied nuclei spans several standard valence spaces used in shell model calculations. These include sd (F, Na, Si), $sdpf$ (Ar), f_5pg_9 (Ge) valence spaces, as well as the valence space with orbits in the major shell between 50 and 82 magic numbers for iodine and xenon. Several interactions are available in each valence space that are usually obtained from different fitting protocols. In addition, valence space restrictions are sometimes used to make the shell model calculations more feasible. Various nuclear shell model interactions were then used for each valence space considered to evaluate uncertainties from ground-state wave functions on nuclear responses. These sometimes lead to significant variations in subleading nuclear responses, usually increasing with the number of nucleons. Although the variations for the LD (Δ) subleading responses remain relatively small (from $\lesssim 10\%$ in sd and f_5pg_9 nuclei to $\sim 30\%$ in ^{127}I and Xe), these are more significant for SD responses (Σ' and Σ''), going from $\lesssim 20\%$ in sd nuclei up to a factor ~ 3 in ^{127}I and Xe. Even larger variations are found in LSD (Φ'') subleading responses, going from $\lesssim 25\%$ (sd) and $\lesssim 65\%$ ($sdpf$), up to factors $\lesssim 5$ (f_5pg_9) and $\lesssim 6$ (^{127}I and Xe). The effect of valence space truncation on the nuclear responses is also non-negligible and should be accounted for as a source of uncertainty. To evaluate the effect of truncation, we first examined two calculations with the SN100PN interaction, one more severe than the other. This produced a factor of ~ 3 difference in the ^{127}I proton SD responses. As a second case, now with the GCN5082 interaction, two more comparable truncations were evaluated. This produced smaller differences of $\sim 20\%$–30% in the subleading proton Σ', Σ'', and Δ channels. These uncertainties should be taken into account when determining possible parameter spaces of NREFT operators from comparison with experiment (see, e.g., [71]).

ACKNOWLEDGMENTS

Valuable discussions with J. Newstead are acknowledged. This research was supported by the Australian Government through the Australian Research Council Centre of Excellence for Dark Matter Particle Physics (CDM, CE200100008).

APPENDIX A: ISOTOPE NUCLEAR STRUCTURE

Here, we present the experimental energy spectra plotted against the theoretical shell model predictions, in addition to tables comparing the theoretical and experimental electric quadrupole and magnetic dipole moments and transitions. This is done for the odd isotopes for which this information is not presented in Sec. III. The model space and shell model interactions considered for the isotopes below are as presented in Sec. IV B.

1. ^{29}Si

The experimental energy levels for ^{29}Si are compared with the theoretical shell model values for the USD and USDB interactions in Fig. 23, for an unrestricted model space. The experimental energy values are well-reproduced by the shell model calculations, in particular for levels up to ~3 MeV.

The effective g factors and charges employed in the electric quadrupole and magnetic dipole values comparison are the same as those used for ^{19}F and ^{23}Na. The electric quadrupole and magnetic dipole values are presented in Table V. Here, the ground state $1/2^+$ does not have an

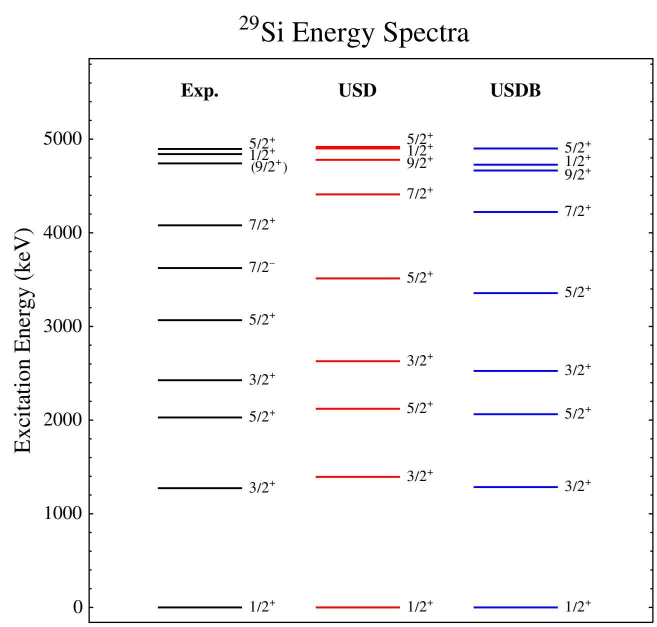

FIG. 23. Same as Fig. 1 for ^{29}Si.

TABLE V. Magnetic dipole moment, and electric quadrupole [B(E2)] and magnetic dipole [B(M1)] transitions, between low-lying states of ^{29}Si. Experimental transition values are from [72], while moment are taken from [54].

	μ [nm]			B(E2) [e^2 fm^4]			B(M1) [nm^2]		
State/Transition	USD	USDB	Exp.	USD	USDB	Exp.	USD	USDB	Exp.
$1/2^+_{gs}$	−0.510	−0.519	−0.555[a]						
$3/2^+_1 \to 1/2^+_{gs}$				34.87	31.02	21.7(21)	0.0223	0.0179	0.0632(23)
$3/2^+_2 \to 1/2^+_{gs}$				30.03	32.55	29.12(1165)	0.2026	0.2057	0.1164(72)

[a]The uncertainty is much less than ±0.001.

electric quadrupole moment. The experimental magnetic dipole moment is in very good agreement with the USD and USDB values for the ground state. Good agreement can also been seen for the electric quadrupole transitions [B(E2)], from the first two excited states to the ground state. The magnetic dipole transition is less well reproduced for these, with factor differences of ~3 and ~2 between experiment and theory.

However, overall agreement between experiment and the shell model calculations is reasonably good, in particular for the nuclear ground-state wave function, which is utilized in the IFF calculations above. USD and USDB should then be suitable interactions for use with ^{29}Si.

2. ^{73}Ge

The JUN45 shell model interaction begins with a realistic interaction based on the Bonn-C potential, where two-body matrix elements and four single-particle energies are modified to fit 400 experimental binding and excitation energy data for 69 nuclei with mass numbers $A = 63$–96. The germanium isotopes relevant for the current work are included in this fit data. For the jj44b interaction, the fit was performed based on 77 binding energies and 470 excitation energies in nuclei with $Z = 28$–30 ($N = 28$–50) and $N = 48$–50 ($Z = 28$–50), and hence does not include these germanium isotopes.

The ^{73}Ge experimental energy spectrum is compared to the shell model values in Fig. 24, using the JUN45 and jj44b interactions in an unrestricted model space. Neither interaction reproduces the experimental energies very well, with the jj44b interaction being considerably less accurate, potentially due to the lack of inclusion of the germanium isotopes in its fitting protocol. The theoretical spectra are not very consistent with each other. However, agreement between experimental and theoretical levels on the order of 200 keV is often considered satisfactory for heavier nuclei.

The experimental magnetic dipole and electric quadrupole moments and transitions are compared to the theoretical values in Tables VI and VII. Here, the effective charges employed are $e_p = 1.8$ and $e_n = 0.8$, whilst the effective g factors are $g_{sp} = 3.910$, $g_{sn} = -2.678$, $g_{lp} = 1.137$, and $g_{ln} = -0.079$. The magnetic moments of the first two states are closer to experiment for the jj44b interaction, compared with the JUN45 values, as is the case for the magnitude of the $5/2^+_1$ electric moment. Both ground-state theoretical electric moments are not very consistent with experiment. The theoretical electric quadrupole transition values are much closer to experiment compared to the magnetic transition counterparts.

Overall, the inconsistency of some aspects of the JUN45 and jj44b interactions with one another and with experimental values indicates a need to improve shell model calculations for the germanium isotopes, in order to obtain more accurate predictions for WIMP-nucleus scattering.

3. ^{129,131}Xe

The experimental and theoretical energies are plotted against one another in Fig. 25 for ^{129}Xe and in Fig. 26 for ^{131}Xe. In both cases the SN100PN interaction was used for the shell model calculations, where the valence space was restricted for ^{129}Xe but left unrestricted for ^{131}Xe. For ^{129}Xe, the ordering of the first two states is consistent between

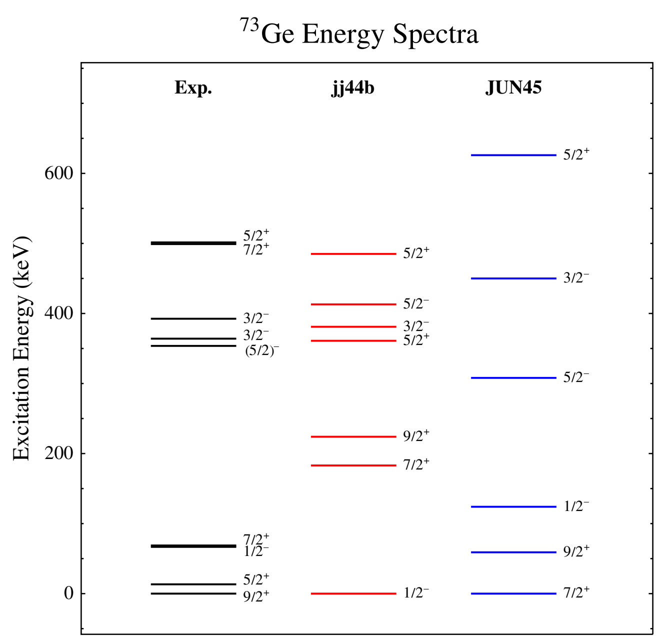

FIG. 24. ^{73}Ge energy spectra (keV) for experimental data, as well as the jj44b and JUN45 interactions in an unrestricted model space.

TABLE VI. Magnetic dipole and electric quadrupole moments of low-lying states of ^{73}Ge. Experimental moments are taken from [54–56].

	Q [e fm^2]			μ [nm]		
State	JUN45	jj44b	Exp.	JUN45	jj44b	Exp.
$9/2^+_{gs}$	−24.94	−11.66	−19.6(1)	−1.22107	−1.0182	−0.87824 [a]
$5/2^+_1$	+15.62	+50.43	70(8) [b]	−1.62940	−0.9484	−1.08(3)

[a]The uncertainty is less than ±0.001.
[b]Sign not specified.

TABLE VII. Electric quadrupole [B(E2)] and magnetic dipole [B(M1)] transitions between low-lying states of ^{73}Ge. Experimental transition values are from [73].

	B(E2) [e^2 fm^4]			B(M1) [nm^2]		
Transition	JUN45	jj44b	Exp.	JUN45	jj44b	Exp.
$5/2^+_1 \to 9/2^+_{gs}$	531.3	556.5	441.8(76)			
$7/2^+_1 \to 9/2^+_{gs}$	605.3	931.1	906.1(1087)	0.004034	0.00002011	0.054774(3401)

experiment and theory, however the shell model spectrum is much more compressed, which could be due to the valence space truncation employed. This compression is not observed in the ^{131}Xe spectrum. Although the ordering of the ^{131}Xe theoretical energy levels is not perfectly consistent with experiment, the predicted low-lying states of a given spin and parity are within 100 keV of experiment.

The shell model magnetic dipole and electric quadrupole moments are displayed against the experimental values in Table VIII. The effective charges and g factors employed are the same as those for ^{127}I. The theoretical magnetic moments for the ground states of both ^{129,131}Xe reproduce well the experimental counterparts, as is the case for the ^{129}Xe electric moment for the $3/2^+_1$ state. The ^{131}Xe ground-state electric moment is not consistent with the experimental value.

Despite the complexity of the low-energy spectra of the odd xenon isotopes in consideration here, the SN100PN shell model interaction overall reproduces reasonably well some features of the spectra as well as moments.

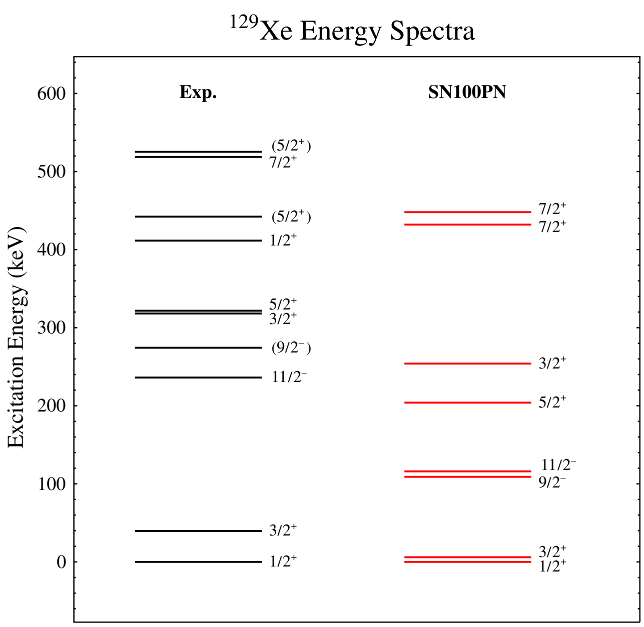

FIG. 25. ^{129}Xe energy spectra (keV) for experimental data, as well as the SN100PN interaction in a restricted model space.

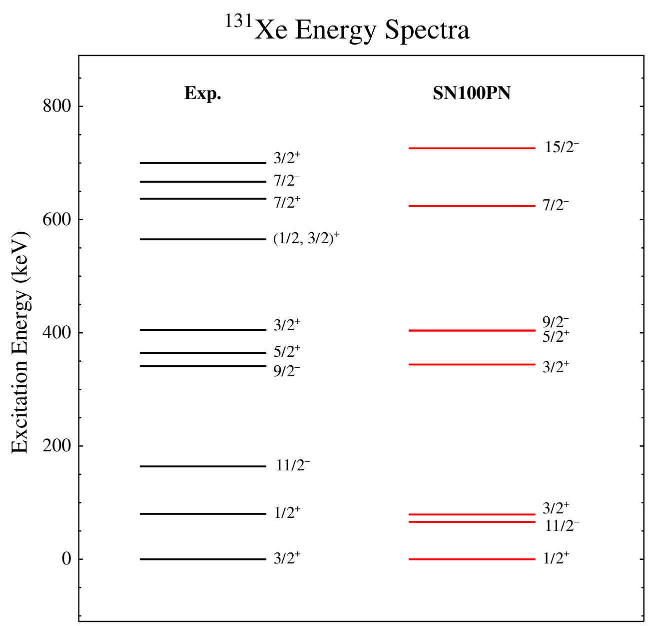

FIG. 26. ^{131}Xe energy spectra (keV) for experimental data, as well as the SN100PN interaction in an unrestricted model space.

TABLE VIII. Magnetic dipole and electric quadrupole moments for low-lying states of ^{129,131}Xe. Experimental moments are taken from [54–56].

		Q [e fm^2]		μ [nm]	
Nucleus	State/Transition	SN100PN	Exp.	SN100PN	Exp.
^{129}Xe	$1/2^+_{\mathrm{gs}}$			−0.872	−0.778[a]
	$3/2^+_1$	−37.48	−39.3(10)	+0.893	+0.58(8)
^{131}Xe	$3/2^+_{\mathrm{gs}}$	+0.69	−11.4(1)	+0.755	+0.692[a]

[a]The uncertainty is much less than ±0.001.

Importantly, the ground-state magnetic moments are reproduced. This interaction can be considered suitable for use in the nuclear response function calculations.

APPENDIX B: EFT AND DM-NUCLEUS ELASTIC SCATTERING FORMALISM

The general expression for the DM-nucleus scattering amplitude is given by [15,16]

$$\begin{aligned}
\frac{1}{2J_i+1}\sum_{M_i,M_f}|\langle J_iM_f|\mathcal{H}_{\mathrm{int}}|J_iM_i\rangle|^2 &= \frac{4\pi}{2J_i+1}\Bigg[\sum_{J=1,3,\ldots}^{\infty}|\langle J_i||\vec{l}_5\cdot\hat{q}\Sigma''_J(q)||J_i\rangle|^2 \\
&+\sum_{J=0,2,\ldots}^{\infty}\Bigg\{|\langle J_i||l_0M_J(q)||J_i\rangle|^2+|\langle J_i||\vec{l}_E\cdot\hat{q}\frac{q}{m_N}\Phi''_J(q)||J_i\rangle|^2 \\
&+2\mathrm{Re}\left[\langle J_i||\vec{l}_E\cdot\hat{q}\frac{q}{m_N}\Phi''_J(q)||J_i\rangle\langle J_i||l_0M_J(q)||J_i\rangle^*\right]\Bigg\} \\
&+\frac{q^2}{2m_N^2}\sum_{J=2,4,\ldots}^{\infty}(\langle J_i||\vec{l}_E\tilde{\Phi}'_J(q)||J_i\rangle\cdot\langle J_i||\vec{l}_E\tilde{\Phi}'_J(q)||J_i\rangle^*-|\langle J_i||\vec{l}_E\cdot\hat{q}\tilde{\Phi}'_J(q)||J_i\rangle|^2) \\
&+\sum_{J=1,3,\ldots}^{\infty}\Bigg\{\frac{q^2}{2m_N^2}(\langle J_i||\vec{l}_M\Delta_J(q)||J_i\rangle\cdot\langle J_i||\vec{l}_M\Delta_J(q)||J_i\rangle^*-|\langle J_i||\vec{l}_M\cdot\hat{q}\Delta_J(q)||J_i\rangle|^2) \\
&+\frac{1}{2}(\langle J_i||\vec{l}_5\Sigma'_J(q)||J_i\rangle\cdot\langle J_i||\vec{l}_5\Sigma'_J(q)||J_i\rangle^*-|\langle J_i||\vec{l}_5\cdot\hat{q}\Sigma'_J(q)||J_i\rangle|^2) \\
&+\mathrm{Re}\left[i\hat{q}\cdot\langle J_i||\vec{l}_M\frac{q}{m_N}\Delta_J(q)||J_i\rangle\times\langle J_i||\vec{l}_5\Sigma'_J(q)||J_i\rangle^*\right]\Bigg\}\Bigg], \qquad \text{(B1)}
\end{aligned}$$

where m_N is the nucleon mass, we have averaged over initial nuclear spins and summed over final ones, and the four DM scattering amplitudes $l_j \equiv l_{0,E,M,5}$ are given by

$$\begin{aligned}
l_0 &= (c_1^0+c_1^1\tau_3)-i(\vec{q}\times\vec{S}_\chi)\cdot\vec{v}_T^\perp(c_5^0+c_5^1\tau_3)+\vec{S}_\chi\cdot\vec{v}_T^\perp(c_8^0+c_8^1\tau_3)+i\vec{q}\cdot\vec{S}_\chi(c_{11}^0+c_{11}^1\tau_3) \\
\vec{l}_5 &= \frac{1}{2}[i\vec{q}\times\vec{v}_T^\perp(c_3^0+c_3^1\tau_3)+\vec{S}_\chi(c_4^0+c_4^1\tau_3)+\vec{S}_\chi\cdot\vec{q}\,\vec{q}(c_6^0+c_6^1\tau_3)+\vec{v}_T^\perp(c_7^0+c_7^1\tau_3) \\
&\quad+i\vec{q}\times\vec{S}_\chi(c_9^0+c_9^1\tau_3)+i\vec{q}(c_{10}^0+c_{10}^1\tau_3)+\vec{v}_T^\perp\times\vec{S}_\chi(c_{12}^0+c_{12}^1\tau_3) \\
&\quad+i\vec{q}\vec{v}_T^\perp\cdot\vec{S}_\chi(c_{13}^0+c_{13}^1\tau_3)+i\vec{v}_T^\perp\vec{q}\cdot\vec{S}_\chi(c_{14}^0+c_{14}^1\tau_3)+\vec{q}\times\vec{v}_T^\perp\vec{q}\cdot\vec{S}_\chi(c_{15}^0+c_{15}^1\tau_3)] \\
\vec{l}_M &= i\vec{q}\times\vec{S}_\chi(c_5^0+c_5^1\tau_3)-\vec{S}_\chi(c_8^0+c_8^1\tau_3) \\
\vec{l}_E &= \frac{1}{2}[\vec{q}(c_3^0+c_3^1\tau_3)+i\vec{S}_\chi(c_{12}^0+c_{12}^1\tau_3)-\vec{q}\times\vec{S}_\chi(c_{13}^0+c_{13}^1\tau_3)-i\vec{q}\,\vec{q}\cdot\vec{S}_\chi(c_{15}^0+c_{15}^1\tau_3)]. \qquad \text{(B2)}
\end{aligned}$$

Here, $\vec{v}_T^\perp=\frac{1}{2}(\vec{v}_{\chi,\mathrm{in}}+\vec{v}_{\chi,\mathrm{out}}-\vec{v}_{T,\mathrm{in}}-\vec{v}_{T,\mathrm{out}})=\vec{v}_T+\frac{\vec{q}}{2\mu_T}$, and $\vec{v}_{T,\mathrm{in(out)}}=\frac{1}{A}\sum_{j=1}^{A}\vec{v}_{N,\mathrm{in(out)}}(j)$.

The Wigner-Eckart theorem has been used to express matrix elements in reduced form, using the convention,

$$\langle j'm'|T_{JM}|jm\rangle = (-1)^{j'-m'}\begin{pmatrix} j' & J & j \\ -m' & M & m \end{pmatrix}\langle j'||T_J||j\rangle. \tag{B3}$$

The nuclear operators present in Eq. (B1) have the form,

$$\begin{aligned}
\Delta_{JM}(q\vec{x}) &\equiv \vec{M}^M_{JJ}(q\vec{x})\cdot\frac{1}{q}\overrightarrow{\nabla},\\
\Sigma'_{JM}(q\vec{x}) &\equiv -i\left[\frac{\overrightarrow{\nabla}}{q}\times\vec{M}^M_{JJ}(q\vec{x})\right]\cdot\vec{\sigma}_N = [J]^{-1}[-\sqrt{J}\vec{M}^M_{JJ+1}(q\vec{x}) + \sqrt{J+1}\vec{M}^M_{JJ-1}(q\vec{x})]\cdot\vec{\sigma}_N,\\
\Sigma''_{JM}(q\vec{x}) &\equiv \left[\frac{\overrightarrow{\nabla}}{q}M_{JM}(q\vec{x})\right]\cdot\vec{\sigma}_N = [J]^{-1}[\sqrt{J+1}\vec{M}^M_{JJ+1}(q\vec{x}) + \sqrt{J}\vec{M}^M_{JJ-1}(q\vec{x})]\cdot\vec{\sigma}_N,\\
\tilde{\Phi}'_{JM}(q\vec{x}) &\equiv \left(\frac{\overrightarrow{\nabla}}{q}\times\vec{M}^M_{JJ}(q\vec{x})\right)\cdot\left(\vec{\sigma}_N\times\frac{1}{q}\overrightarrow{\nabla}\right) + \frac{1}{2}\vec{M}^M_{JJ}(q\vec{x})\cdot\vec{\sigma}_N,\\
\Phi''_{JM}(q\vec{x}) &\equiv i\left(\frac{\overrightarrow{\nabla}}{q}M_{JM}(q\vec{x})\right)\cdot\left(\vec{\sigma}_N\times\frac{1}{q}\overrightarrow{\nabla}\right),
\end{aligned} \tag{B4}$$

where $M_{JM}(q\vec{x}) \equiv j_J(qx)Y_{JM}(\Omega_x)$, $\vec{M}^M_{JL} \equiv j_L(qx)\vec{Y}_{JLM}$, $[J] = \sqrt{2J+1}$, and $\vec{\sigma}_N$ is the nucleon spin operator. Here, $j_J(qx)$ is the spherical Bessel function, Y_{JM} is the spherical harmonic, and $\vec{Y}_{JLM}$ is the vector spherical harmonic. The following spherical harmonic and vector spherical harmonic identities are also employed in the derivation,

$$\begin{aligned}
e^{i\vec{q}.\vec{x}_i} &= \sum_{J=0}^{\infty}\sqrt{4\pi}[J](i)^J j_J(qx_i)Y_{J0}(\Omega_{x_i}),\\
\hat{e}_\lambda e^{i\vec{q}.\vec{x}_i} &= \begin{cases} \sum_{J=0}{}^{\infty}\sqrt{4\pi}[J](i)^{J-1}\frac{\vec{\nabla}_i}{q}(j_J(qx_i)Y_{J0}(\Omega_{x_i})), & \text{for } \lambda = 0 \\ \sum_{J\geq 1}{}^{\infty}\sqrt{2\pi}[J](i)^{J-2}\left[\lambda j_J(qx_i)\vec{Y}^\lambda_{JJ1}(\Omega_{x_i}) + \frac{\overrightarrow{\nabla}_i}{q}\times(j_J(qx_i)\vec{Y}^\lambda_{JJ1}(\Omega_{x_i}))\right], & \text{for } \lambda = \pm 1. \end{cases}
\end{aligned} \tag{B5}$$

APPENDIX C: NUSHELLX AND OBDMEs

1. Valence OBDMEs

The OBDME values provided by NuShellX are in proton-neutron (pn) formalism, and have the form,

$$\frac{\langle J_f|||[a^\dagger_{|\alpha|N}\bar{a}_{|\beta|N}]_J||J_i\rangle}{\sqrt{2J+1}} \equiv \frac{a(NN)}{\sqrt{2J+1}}, \tag{C1}$$

where $\bar{a}_\beta = (-1)^{j_\beta - m_{j_\beta}}a_{|\beta|;-m_{j_\beta}}$ and $N = \{p, n\}$. This is converted to isospin formalism to be used with the previous expressions through,

$$\begin{aligned}
\Psi^{J;\tau}_{|\alpha|,|\beta|} &\equiv \frac{\langle J_i;T\vdots\vdots[a^\dagger_{|\alpha|}\otimes\tilde{a}_{|\beta|}]_{J;\tau}\vdots\vdots J_i;T\rangle}{\sqrt{(2J+1)(2\tau+1)}}\\
&= \frac{(-1)^{-\tau-2J}\sqrt{2T+1}}{\sqrt{(2J+1)(2\tau+1)}C^{TM_T}_{\tau 0;TM_T}}[C^{\tau 0}_{1/21/2;1/2-1/2}a(pp) - C^{\tau 0}_{1/2-1/2;1/21/2}a(nn)],
\end{aligned} \tag{C2}$$

where $C^{j'm'}_{kq;jm} \equiv \langle kqjm|j'm'\rangle$ are Clebsch-Gordan (CG) coefficients.

For $\tau = 0$ and $\tau = 1$ the conversion becomes,

$$\Psi^{J;0}_{|\alpha|,|\beta|} = \frac{\sqrt{2T+1}(a(pp)+a(nn))}{\sqrt{2(2J+1)}C^{TM_T}_{00;TM_T}}, \tag{C3}$$

and

$$\Psi^{J;1}_{|\alpha|,|\beta|} = \frac{\sqrt{2T+1}(-a(pp)+a(nn))}{\sqrt{6(2J+1)}C^{TM_T}_{10;TM_T}}. \tag{C4}$$

The coefficients $\sqrt{2T+1}/C^{TM_T}_{00;TM_T}$ and $\sqrt{2T+1}/C^{TM_T}_{10;TM_T}$ are both isospin-dependent, and hence must be calculated separately for each isotope considered.

2. Core OBDMEs

The above OBDMEs provided by NuShellX only describe the valence single-particle orbitals. Equation (5) also needs to be evaluated for orbitals within the filled core. It can be shown that the OBDME expression for core states has the form,

$$\begin{aligned}\Psi^{J;\tau}_{|\beta|,|\beta|} &= \sum_{M_i,m_{j_\beta},m_{t_\beta}} \frac{(-1)^{j_\beta-m_{j_\beta}+t_\beta-m_{t_\beta}}(-1)^{\tau+J}C^{J0}_{j_\beta m_{j_\beta};j_\beta-m_{j_\beta}}C^{\tau0}_{t_\beta m_{t_\beta};t_\beta-m_{t_\beta}}\sqrt{2T+1}}{C^{TM_T}_{\tau0;TM_T}C^{J_iM_i}_{J0;J_iM_i}\sqrt{(2J+1)(2\tau+1)(2J_i+1)}}, \\ &= \sqrt{2(2J_i+1)(2T+1)(2j_\beta+1)},\end{aligned} \tag{C5}$$

where M_i is the projection of the angular momentum J_i, and $t_\beta = 1/2$.

APPENDIX D: MATHEMATICA PACKAGE AND DENSITY MATRIX SYNTAX

This work employs the Mathematica package provided by [16] to calculate the nuclear form factors presented above. Among its various functions, this script computes (in isospin formalism) the nuclear response functions,

$$W^{\tau\tau'}_{X,Y}(y) \equiv \sum_J \langle J_i||X_{J;\tau}(q)||J_i\rangle\langle J_i||Y_{J;\tau'}(q)||J_i\rangle, \tag{D1}$$

where $W^{\tau\tau'}_X(y) \equiv W^{\tau\tau'}_{X,X}(y)$, and $\tau = 0(1)$ indicates isospin-independence (dependence). Linear combinations of the functions (D1) give the nuclear response functions in proton-neutron formalism required in Eq. (7). These nuclear response functions are given by the script function `ResponseNuclear [y, i, tau, tau2]` where i takes on values from 1 to 8, to give W_M, $W_{\Sigma''}$, $W_{\Sigma'}$, $W_{\Phi''}$, $W_{\tilde{\Phi}'}$, W_Δ, $W_{M\Phi''}$, and $W_{\Sigma'\Delta}$, respectively.

The package provides these functions for the default density matrices $\Psi^{J,\tau}(|\alpha|,|\beta|)$ employed to calculate the results presented in [15,16], for the nuclear isotopes ^{19}F, ^{23}Na, ^{28,29,30}Si, ^{70,72,73,74,76}Ge, ^{127}I, and ^{128,129,130,131,132,134,136}Xe. These can be called on using `SetIsotope [Z, A, bFM, filename]` with filename=“default”. However, custom density matrices can be loaded into the script through a custom file, whose format must follow that provided in [16]. We provide these density matrix files as part of the supplementary material [43] in the appropriate format for use with the aforementioned Mathematica package, with density matrix values obtained from our own nuclear shell model calculations for ^{19}F, ^{23}Na, ^{28,29,30}Si, ^{40}Ar, ^{70,72,73,74,76}Ge, ^{127}I, and ^{128,129,130,131,132,134,136}Xe.

[1] G. Bertone and D. Hooper, Rev. Mod. Phys. **90**, 045002 (2018).
[2] J. L. Feng, Annu. Rev. Astron. Astrophys. **48**, 495 (2010).
[3] T. Marrodán Undagoitia and L. Rauch, J. Phys. G **43**, 013001 (2016).
[4] J. Liu, X. Chen, and X. Ji, Nat. Phys. **13**, 212 (2017).
[5] G. Jungman, M. Kamionkowski, and K. Griest, Phys. Rep. **267**, 195 (1996).
[6] M. Schumann, J. Phys. G **46**, 103003 (2019).
[7] L. Roszkowski, E. M. Sessolo, and S. Trojanowski, Rep. Prog. Phys. **81**, 066201 (2018).
[8] G. Arcadi, M. Dutra, P. Ghosh, M. Lindner, Y. Mambrini, M. Pierre, S. Profumo, and F. S. Queiroz, Eur. Phys. J. C **78**, 203 (2018).
[9] J. M. Gaskins, Contemp. Phys. **57**, 496 (2016).
[10] G. D'Imperio (SABRE Collaboration), J. Phys. Conf. Ser. **1342**, 012060 (2020).
[11] J. Amare *et al.*, Phys. Rev. D **103**, 102005 (2021).
[12] G. Adhikari *et al.* (COSINE-100 Collaboration), Sci. Adv. **7**, abk2699 (2021).
[13] R. Bernabei *et al.*, Universe **4**, 116 (2018).
[14] J. Engel, S. Pittel, and P. Vogel, Int. J. Mod. Phys. E **1**, 1 (1992).

[15] A. L. Fitzpatrick, W. Haxton, E. Katz, N. Lubbers, and Y. Xu, J. Cosmol. Astropart. Phys. 02 (2013) 004.
[16] N. Anand, A. L. Fitzpatrick, and W. C. Haxton, Phys. Rev. C **89**, 065501 (2014).
[17] M. Hoferichter, P. Klos, and A. Schwenk, Phys. Lett. B **746**, 410 (2015).
[18] M. Hoferichter, P. Klos, J. Menéndez, and A. Schwenk, Phys. Rev. D **94**, 063505 (2016).
[19] M. Hoferichter, P. Klos, J. Menéndez, and A. Schwenk, Phys. Rev. D **99**, 055031 (2019).
[20] L. Vietze, P. Klos, J. Menéndez, W. C. Haxton, and A. Schwenk, Phys. Rev. D **91**, 043520 (2015).
[21] P. Klos, J. Menéndez, D. Gazit, and A. Schwenk, Phys. Rev. D **88**, 083516 (2013); **89**, 029901(E) (2014).
[22] J. Menendez, D. Gazit, and A. Schwenk, Phys. Rev. D **86**, 103511 (2012).
[23] T. R. Richardson, X. Lin, and S. T. Nguyen, Phys. Rev. C **106**, 044003 (2022).
[24] G. Adhikari *et al.* (COSINE-100 Collaboration), Phys. Rev. D **106**, 052005 (2022).
[25] E. Aprile *et al.* (XENON Collaboration), Phys. Rev. Lett. **131**, 041003 (2023).
[26] J. Aalbers *et al.* (LZ Collaboration), Phys. Rev. Lett. **131**, 041002 (2023).
[27] Y. Meng *et al.* (PandaX-4T Collaboration), Phys. Rev. Lett. **127**, 261802 (2021).
[28] K. Abe *et al.* (XMASS Collaboration), Phys. Rev. D **108**, 083022 (2023).
[29] M. Lai (DEAP-3600 Collaboration), J. Instrum. **18**, C02046 (2023).
[30] R. Agnese *et al.* (SuperCDMS Collaboration), Phys. Rev. D **97**, 022002 (2018).
[31] J. Fan, M. Reece, and L.-T. Wang, J. Cosmol. Astropart. Phys. 11 (2010) 042.
[32] X. G. Wang and A. W. Thomas, Phys. Rev. C **103**, 034606 (2021).
[33] H. Hergert, Front. Phys. **8**, 379 (2020).
[34] D. Gazda, R. Catena, and C. Forssén, Phys. Rev. D **95**, 103011 (2017).
[35] C. Körber, A. Nogga, and J. de Vries, Phys. Rev. C **96**, 035805 (2017).
[36] L. Andreoli, V. Cirigliano, S. Gandolfi, and F. Pederiva, Phys. Rev. C **99**, 025501 (2019).
[37] B. S. Hu, J. Padua-Argüelles, S. Leutheusser, T. Miyagi, S. R. Stroberg, and J. D. Holt, Phys. Rev. Lett. **128**, 072502 (2022).
[38] A. E. Stuchbery and J. L. Wood, MDPI Phys. **4**, 697 (2022).
[39] J. M. R. Fox, C. W. Johnson, and R. Navarro Perez, Phys. Rev. C **108**, 054310 (2023).
[40] S. Yoshida, N. Shimizu, T. Togashi, and T. Otsuka, Phys. Rev. C **98**, 061301 (2018).
[41] M. Horoi, A. Neacsu, and S. Stoica, Phys. Rev. C **107**, 045501 (2023).
[42] D. J. Heimsoth, B. Lem, A. M. Suliga, C. W. Johnson, A. B. Balantekin, and S. N. Coppersmith, Phys. Rev. D **108**, 103031 (2023).
[43] See Supplemental Material at http://link.aps.org/supplemental/10.1103/PhysRevD.109.075036 for an extended discussion of the calculations presented in this work.
[44] T. De Forest, Jr. and J. D. Walecka, Adv. Phys. **15**, 1 (1966).
[45] T. W. Donnelly and J. D. Walecka, Annu. Rev. Nucl. Part. Sci. **25**, 329 (1975).
[46] B. D. Serot, Nucl. Phys. **A322**, 408 (1979).
[47] J. S. O' Connell, T. W. Donnelly, and J. D. Walecka, Phys. Rev. C **6**, 719 (1972).
[48] T. W. Donnelly and W. C. Haxton, At. Data Nucl. Data Tables **23**, 103 (1979).
[49] B. A. Brown and W. D. M. Rae, Nucl. Data Sheets **120**, 115 (2014).
[50] B. A. Brown and B. H. Wildenthal, Annu. Rev. Nucl. Part. Sci. **38**, 29 (1988).
[51] B. H. Wildenthal, Prog. Part. Nucl. Phys. **11**, 5 (1984).
[52] B. A. Brown and W. A. Richter, Phys. Rev. C **74**, 034315 (2006).
[53] W. A. Richter, S. Mkhize, and B. A. Brown, Phys. Rev. C **78**, 064302 (2008).
[54] N. J. Stone, Table of recommended nuclear magnetic dipole moments: Part I—long-lived states, International Atomic Energy Agency (IAEA) Technical Report No. INDC(NDS)-0794, 2019, https://www-nds.iaea.org/publications/indc/indc-nds-0794.pdf.
[55] N. J. Stone, Table of recommended nuclear magnetic dipole Moments—Part II, short-lived states, International Atomic Energy Agency (IAEA) Technical Report No. INDC(NDS)-0816, 2020, https://www-nds.iaea.org/publications/indc/indc-nds-0816.pdf.
[56] N. J. Stone, Table of nuclear electric quadrupole moments, International Atomic Energy Agency (IAEA) Technical Report No. INDC(NDS)-0833, 2021, https://www-nds.iaea.org/publications/indc/indc-nds-0833.pdf.
[57] D. R. Tilley, H. R. Weller, C. M. Cheves, and R. M. Chasteler, Nucl. Phys. **A595**, 1 (1995).
[58] M. Shamsuzzoha Basunia and A. Chakraborty, Nucl. Data Sheets **171**, 1 (2021).
[59] W. J. Baldridge and B. J. Dalton, Phys. Rev. C **18**, 539 (1978).
[60] B. A. Brown, N. J. Stone, J. R. Stone, I. S. Towner, and M. Hjorth-Jensen, Phys. Rev. C **71**, 044317 (2005); **72**, 029901(E) (2005).
[61] J. Menendez, A. Poves, E. Caurier, and F. Nowacki, Nucl. Phys. **A818**, 139 (2009).
[62] R. Machleidt, Phys. Rev. C **63**, 024001 (2001).
[63] S. F. Hicks *et al.*, Phys. Rev. C **105**, 024329 (2022).
[64] J. D. Lewin and P. F. Smith, Astropart. Phys. **6**, 87 (1996).
[65] S. Nummela *et al.*, Phys. Rev. C **63**, 044316 (2001).
[66] F. Nowacki and A. Poves, Phys. Rev. C **79**, 014310 (2009).
[67] K. Kaneko, Y. Sun, T. Mizusaki, and M. Hasegawa, Phys. Rev. C **83**, 014320 (2011).
[68] Y. Utsuno, T. Otsuka, B. A. Brown, M. Honma, T. Mizusaki, and N. Shimizu, Phys. Rev. C **86**, 051301 (2012).
[69] M. Honma, T. Otsuka, T. Mizusaki, and M. Hjorth-Jensen, Phys. Rev. C **80**, 064323 (2009).
[70] S. Mukhopadhyay, B. P. Crider, B. A. Brown, S. F. Ashley, A. Chakraborty, A. Kumar, M. T. McEllistrem, E. E. Peters, F. M. Prados-Estévez, and S. W. Yates, Phys. Rev. C **95**, 014327 (2017).
[71] M. Cirelli, E. Del Nobile, and P. Panci, J. Cosmol. Astropart. Phys. 10 (2013) 019.
[72] M. Shamsuzzoha Basunia, Nucl. Data Sheets **113**, 909 (2012).
[73] B. Singh and J. Chen, Nucl. Data Sheets **158**, 1 (2019).